

# A fast radio burst source at a complex magnetised site in a barred galaxy

H. Xu<sup>1,2,3</sup>, J. R. Niu<sup>2,4</sup>, P. Chen<sup>1,3,5</sup>, K. J. Lee<sup>1,2\*</sup>, W. W. Zhu<sup>2†</sup>, S. Dong<sup>1‡</sup>, B. Zhang<sup>6,7§</sup>, J. C. Jiang<sup>1,2,3</sup>, B. J. Wang<sup>1,2,3</sup>, J. W. Xu<sup>1,2,3</sup>, C. F. Zhang<sup>1,2,3</sup>, H. Fu<sup>8</sup>, A. V. Filippenko<sup>9</sup>, E. W. Peng<sup>3,1</sup>, D. J. Zhou<sup>2,4</sup>, Y. K. Zhang<sup>2,4</sup>, P. Wang<sup>2</sup>, Y. Feng<sup>2,10</sup>, Y. Li<sup>11</sup>, T. G. Brink<sup>9</sup>, D. Z. Li<sup>12</sup>, W. Lu<sup>13</sup>, Y. P. Yang<sup>14</sup>, R. N. Caballero<sup>1</sup>, C. Cai<sup>15</sup>, M. Z. Chen<sup>16</sup>, Z. G. Dai<sup>17</sup>, S. G. Djorgovski<sup>18</sup>, A. Esamdin<sup>16</sup>, H. Q. Gan<sup>2</sup>, P. Guhathakurta<sup>19</sup>, J. L. Han<sup>2</sup>, L. F. Hao<sup>20</sup>, Y. X. Huang<sup>20</sup>, P. Jiang<sup>2</sup>, C. K. Li<sup>15</sup>, D. Li<sup>2,21</sup>, H. Li<sup>2</sup>, X. Q. Li<sup>15</sup>, Z. X. Li<sup>20</sup>, Z. Y. Liu<sup>16</sup>, R. Luo<sup>22</sup>, Y. P. Men<sup>23</sup>, C. H. Niu<sup>2</sup>, W. X. Peng<sup>15</sup>, L. Qian<sup>2</sup>, L. M. Song<sup>15</sup>, D. Stern<sup>24</sup>, A. Stockton<sup>25</sup>, J. H. Sun<sup>2</sup>, F. Y. Wang<sup>26</sup>, M. Wang<sup>20</sup>, N. Wang<sup>16</sup>, W. Y. Wang<sup>3</sup>, X. F. Wu<sup>11</sup>, S. Xiao<sup>15</sup>, S. L. Xiong<sup>15</sup>, Y. H. Xu<sup>20</sup>, R. X. Xu<sup>3,1,27</sup>, J. Yang<sup>26</sup>, X. Yang<sup>11</sup>, R. Yao<sup>2</sup>, Q. B. Yi<sup>15</sup>, Y. L. Yue<sup>2</sup>, D. J. Yu<sup>2</sup>, W. F. Yu<sup>30</sup>, J. P. Yuan<sup>16</sup>, B. B. Zhang<sup>26,28</sup>, S. B. Zhang<sup>11</sup>, S. N. Zhang<sup>15</sup>, Y. Zhao<sup>15</sup>, W. K. Zheng<sup>9</sup>, Y. Zhu<sup>2</sup>, J. H. Zou<sup>29,26</sup>

<sup>1</sup>*Kavli Institute for Astronomy and Astrophysics, Peking University, Beijing 100871, P. R. China*

<sup>2</sup>*National Astronomical Observatories, Chinese Academy of Sciences, Beijing 100101, P.R. China*

<sup>3</sup>*Department of Astronomy, Peking University, Beijing 100871, P. R. China*

<sup>4</sup>*University of Chinese Academy of Sciences, Chinese Academy of Sciences, Beijing 100049, P. R. China*

<sup>5</sup>*Department of Particle Physics and Astrophysics, Weizmann Institute of Science, Rehovot 76100, Israel*

<sup>6</sup>*Nevada Center for Astrophysics, University of Nevada, Las Vegas, NV 89154, USA*

<sup>7</sup>*Department of Physics and Astronomy, University of Nevada, Las Vegas, NV 89154, USA*

<sup>8</sup>*Department of Physics & Astronomy, University of Iowa, Iowa City, IA 52242, USA*

<sup>9</sup>*Department of Astronomy, University of California, Berkeley, CA 94720-3411, USA*

<sup>10</sup>*Zhejiang Lab, Hangzhou, Zhejiang 311121, People's Republic of China*

<sup>11</sup>*Purple Mountain Observatory, Chinese Academy of Sciences, Nanjing 210008, P. R. China*

<sup>12</sup>*TAPIR, Walter Burke Institute for Theoretical Physics, Mail Code 350-17, Caltech, Pasadena, CA 91125, USA*

<sup>13</sup>*Department of Astrophysical Sciences, Princeton University, Princeton, NJ 08544, USA*

<sup>14</sup>*South-Western Institute For Astronomy Research, Yunnan University, Yunnan 650504, P. R. China*

<sup>15</sup>*Key laboratory of Particle Astrophysics, Institute of High Energy Physics, Chinese Academy of*

\*E-mail: kjlee@pku.edu.cn, [orcid.org/0000-0002-1435-0883](https://orcid.org/0000-0002-1435-0883)

†Email: zhuww@nao.cas.cn, [orcid.org/0000-0001-5105-4058](https://orcid.org/0000-0001-5105-4058)

‡Email: dongsubo@pku.edu.cn, [orcid.org/0000-0002-1027-0990](https://orcid.org/0000-0002-1027-0990)

§Email: bing.zhang@unlv.edu, [orcid.org/0000-0002-9725-2524](https://orcid.org/0000-0002-9725-2524)

Sciences, Beijing 100049, P.R. China

<sup>16</sup>Xinjiang Astronomical Observatory, Chinese Academy of Sciences, Urumqi 830011, P. R. China

<sup>17</sup>University of Science and Technology of China, Anhui 230026, P. R. China.

<sup>18</sup>Division of Physics, Mathematics, and Astronomy, California Institute of Technology, Pasadena, CA 91125, USA.

<sup>19</sup>UCO/Lick Observatory, Department of Astronomy & Astrophysics, University of California Santa Cruz, 1156 High Street, Santa Cruz, CA 95064, USA

<sup>20</sup>Yunnan Observatories, Chinese Academy of Sciences, Kunming 650216, P. R. China

<sup>21</sup>Guizhou Normal University, Guiyang 550001, P. R. China

<sup>22</sup>CSIRO Space and Astronomy, Epping, NSW 1710, Australia

<sup>23</sup>Max-Planck institut für Radioastronomie, Auf Dem Hügel, Bonn, 53121, Germany

<sup>24</sup>Jet Propulsion Laboratory, California Institute of Technology, 4800 Oak Grove Drive, Pasadena, CA 91109, USA

<sup>25</sup>Institute for Astronomy, University of Hawaii, Honolulu, HI 96822, USA

<sup>26</sup>School of Astronomy and Space Science, Nanjing University, Nanjing 210093, P. R. China

<sup>27</sup>State Key Laboratory of Nuclear Physics and Technology, School of Physics, Peking University, Beijing 100871, P. R. China

<sup>28</sup>Key Laboratory of Modern Astronomy and Astrophysics (Nanjing University), Ministry of Education, P. R. China

<sup>29</sup>College of Physics, Hebei Normal University, Shijiazhuang 050024, P. R. China

<sup>30</sup>Shanghai Astronomical Observatory, Chinese Academy of Sciences, Shanaghai 200030, P. R. China

**Fast radio bursts (FRBs) are highly dispersed millisecond-duration radio bursts<sup>1-3</sup>. Recent observations of a Galactic FRB<sup>4-8</sup> suggest that at least some FRBs originate from magnetars, but the origin of cosmological FRBs is still not settled. Here we report the detection of 1863 bursts in 82 hr over 54 days from the repeating source FRB 20201124A<sup>9</sup>. These observations show irregular short-time variation of the Faraday rotation measure (RM), which probes the density-weighted line-of-sight magnetic field strength, of individual bursts during the first 36 days, followed by a constant RM. We detected circular polarisation in more than half of the burst sample, including one burst reaching a high fractional circular polarisation of 75%. Oscillations in fractional linear and circular polarisations as well as polarisation angle as a function of wavelength were detected. All of these features provide evidence for a complicated, dynamically evolving, magnetised immediate environment within about an astronomical unit (au; Earth-Sun distance) of the source. Our optical observations of its Milky-Way-sized, metal-rich host galaxy<sup>10-12</sup> reveal a barred spiral, with the FRB source re-**

**siding in a low stellar density, interarm region at an intermediate galactocentric distance. This environment is inconsistent with a young magnetar engine formed during an extreme explosion of a massive star that resulted in a long gamma-ray burst or superluminous supernova.**

Triggered by observations of the Canadian Hydrogen Intensity Mapping Experiment<sup>9</sup>, we used the Five-hundred-meter Aperture Spherical radio Telescope (FAST)<sup>13</sup> to monitor FRB 20201124A from 2021 April 1 to June 11 (UT) with 91 hr total observing time. The 19-beam receiver was used to cover the frequency range 1.0–1.5 GHz. Our detection threshold was a signal-to-noise ratio  $S/N > 7$ , and 1103 bright bursts reached  $S/N > 30$  among a total of 1863 detected bursts. The burst flux is 0.005–11.5 Jy, and the inferred isotropic luminosity after integrating signal bandwidth spans from  $5 \times 10^{37}$  erg s<sup>-1</sup> to  $3 \times 10^{40}$  erg s<sup>-1</sup>. The daily burst energy distribution shows no secular trend (Methods), while the burst-to-burst fluctuation exceeds two orders of magnitude.

The daily event rate varies slowly (Figure 1), with minimal and maximal values of  $6 \pm 1$  and  $46 \pm 8$  hr<sup>-1</sup>, respectively. Throughout paper, the error bars are for the 68% confidence level unless otherwise specified. The waiting time follows a bimodal distribution with timescales peaking at 39 ms and 135.2 s (Methods). Similar bimodality in waiting time had also been detected in the repeating FRB 20121102A<sup>14</sup>, which may indicate a common mechanism. The high event rate makes FRB 20201124A among the most active known FRBs. We witnessed the quenching of the burst activity on a timescale  $< 74$  hr, when the source stopped emitting any bursts above the flux limit of 4.3 mJy at the fiducial burst width of 5 ms on 2021 May 29. We continued to observe the source over the next 16 days and did not detect a single burst during the 9 hr of observations (Figure 1). Counterintuitively, the burst rate did not show any sign of a monotonic decrease, but a slow increase from  $6 \pm 1$  hr<sup>-1</sup> to  $27^{+7}_{-8}$  hr<sup>-1</sup> during the last 20 days before the quenching.

FRB 20201124A bursts show diverse polarisation properties, including nearly constant polarisation angle (PA) across the phase<sup>15,16</sup>, significant PA swings<sup>17</sup>, and a high amount of circular polarisation (Figure 2). In our burst sample, 50% of the bright bursts ( $S/N > 30$ ) had circular polarisation higher than 3.3%, while the maximal circular polarisation reaches 75%, higher than the 47% reported previously<sup>18</sup>. This is in contrast to most FRBs<sup>1</sup> or radio-emitting magnetars<sup>19</sup> showing little circular polarisation.

For some bursts with moderate circular polarisation, the frequency spectra of both circular and linear polarisations show oscillating features (e.g., bursts 779 and 926 in Figure 2), which indicate Faraday conversion (i.e., generalised Faraday rotation) or polarisation-dependent absorption. The oscillation phases of the linear and circular polarisations are approximately offset by 180°. We also detected highly circularly polarised bursts without such quasiperiodic structures (burst 1472

in Figure 2). This suggests that there is likely an alternative mechanism for producing circular polarisation in addition to the polarisation oscillations. Since the synchrotron maser model invoking relativistic shocks does not predict circular polarisation, our results support the magnetospheric origin of FRB emission<sup>3,17,20,21</sup>.

The RM shows a stochastic temporal variation between  $-889.5^{+0.7}_{-0.7}$  and  $-365.1^{+2.9}_{-1.4}$   $\text{rad m}^{-2}$ , on a timescale of 10 days (Figure 1) and the largest burst-to-burst RM variation per session with a root-mean-square (RMS) value of  $77.2 \text{ rad m}^{-2}$ . Within a single burst, the profile evolution induced apparent RM variation is  $\sim 15.6 \text{ rad m}^{-2}$ . The detected stochastic RM variations on 10-day timescale are more than 40 times larger, suggesting that stochastic RM variations do not result from the profile evolution. Compared with the case of FRB 20121102A<sup>16,22</sup>, the fractional amplitude of RM variation in FRB 20201124A is larger, while the absolute amplitude is smaller. The RM variation quickly stopped  $\sim 20$  days before the quenching of the radio bursts, with the 95% confidence level upper limit of  $\Delta\text{RM} \leq 9.1 \text{ rad m}^{-2}$ , a factor of 50 smaller than the amplitude of stochastic RM variations detected earlier.

The significant RM variation on a 10-day timescale could be caused by a change of either the magnetic field configuration or the density profile along the line of sight close to the source region. The sub-au size of the Faraday screen is estimated as  $\sim 0.6 \text{ au}(\tau/10\text{d})(v/100 \text{ km s}^{-1})$ , where  $\tau$  is the timescale of RM variation and  $v$  is the relative transverse velocity between the screen and the FRB source. Similar to the FRB 20201124A, the Galactic binary pulsar system PSR B1259–63 shows irregular RM evolution<sup>23</sup>. Thus, the lack of periodicity in RM variation may not rule out the binary scenario, and is probably related to irregular mass ejection from the companion star. The cessation of RM variation suggests that the line of sight is less contaminated by the varying component of the medium density. If the central engine is an isolated young magnetar, the RM is predicted to show a secular monotonic decline with time<sup>24,25</sup>.

The oscillations of the linear and circular polarisation fractions as well as the linear polarisation angle as functions of radio wavelength probe the magnetic field and the relativistic plasma close to the FRB central engine. They are likely a consequence of the polarisation-dependent absorption or conversion, which requires  $B \geq 3(\gamma/10)^{-2}$  Gauss, where  $\gamma$  is the kinetic Lorentz factor of the plasma (Methods). Owing to the burst-to-burst variation of polarisation oscillation phenomena, the distance scale associated with the oscillation in polarisation is  $0.1 \text{ au}(\tau/\text{min})$  assuming that the bursts propagate at the speed of light. The polarisation oscillation suggests that the vicinity of the FRB source is occupied by a variable Gauss-level magnetic field together with both a cold and a relativistic plasma (Methods).

We performed optical and near-infrared observations of the host galaxy SDSS J050803.48+260338.0<sup>10–12</sup>

using the 10 m Keck telescopes, including high- and low-dispersion spectra with the Echellette Spectrograph Imager (ESI) and the Low Resolution Imaging Spectrometer (LRIS), respectively, and  $K'$ -band images with the NIRC2 camera using the laser guide-star adaptive-optics (AO) system. In the optical spectra, we detected multiple emission lines (Figure 3(a)) and derived  $z = 0.09795 \pm 0.00003$ , which corresponds to a luminosity distance of  $453.3 \pm 0.1$  Mpc adopting the standard *Planck* cosmological model<sup>26</sup>. Similar to the hosts of several other repeaters (e.g., FRB 20121102A<sup>27</sup>, FRB 20180916B<sup>28</sup>, FRB 20180301A<sup>29</sup>), this host is in the star-forming branch of the Baldwin-Phillips-Terlevich diagram<sup>30</sup> (Methods). Our adaptive-optics (AO) image (Figure 3(b)), with a full width at half-maximum resolution of  $0.12''$ , shows that the host is a barred galaxy with spiral features, and the FRB's apparent location is in the disc but offset from the bar and spiral arms.

The galaxy's stellar mass<sup>10,11</sup>,  $M_* \approx 3 \times 10^{10} M_\odot$ , is about half that of the Milky Way (MW); in contrast, its star-formation rate ( $\text{SFR} = 3.4 \pm 0.3 M_\odot \text{yr}^{-1}$ ) is about twice that of the MW, and its metallicity ( $12 + \log(\text{O}/\text{H}) = 9.07_{-0.04}^{+0.03}$ ) is approximately twice the solar abundance (Methods). The projected offset of the FRB location from the galaxy centre and the specific SFR appear to be typical compared with known FRB hosts (Methods), and its metallicity is higher than that of any FRB host reported previously (most were for non-repeating FRBs)<sup>31,32</sup>. One active repeater, FRB 20121102A, is hosted by a metal-poor dwarf galaxy with a high specific SFR<sup>27,33</sup>, which is similar to the hosts of long gamma-ray bursts or hydrogen-poor superluminous supernovae. This has motivated a hypothesised connection between active repeating FRBs and young, millisecond magnetars<sup>34</sup>. In contrast, the host of FRB 20201124A is more metal-rich and massive than almost all known hosts of long gamma-ray bursts or hydrogen-poor superluminous supernovae<sup>32</sup>. It has been speculated that FRB 20201124A may reside in a star-forming region in the host galaxy<sup>10-12</sup>. However, the interarm location of the source revealed by our image does not support such a possibility, so a young magnetar engine born from an extreme explosion is disfavoured. Nonetheless, a regular magnetar similar to those in the MW is still possible, although the high burst rate, not seen in the Galactic magnetars, requires unusual intrinsic or environmental conditions.

Figure 1: **Temporal variations of the physical parameters of FRB 20201124A.** (a) Daily number of bursts detected. (b) Weibull event rate (blue) and Poisson event rate (magenta). (c) Daily RM, where the violin symbol indicates the distribution function, the green shaded strips indicate the 95% upper and lower bounds, and the solid black curve is the median. Vertical dashed line indicates MJD 59339, where the largest RM fluctuation is noted. (d) and (e) Fractional linear and circular polarisations measured for each individual burst. (f) Observation length of each day. The grey shaded region on the right side of the plot shows the epoch when no burst was detected.

Figure 2: **Polarisation profiles, dynamic spectra, and frequency-dependent polarisation of selected bursts.** (a) PA curve. (b) Polarisation profile, where total intensity, linear, and circular polarisations normalised to the off-pulse noise of total intensity are in black, red, and blue curves, respectively. (c) Dynamic spectra of total intensity. The horizontal white strips and red markers represent frequency channels that have been removed owing to either radio-frequency interference (RFI) or band edges. (d) Fractional polarisation as a function of the square of wavelength, where green, magenta, and blue dots and error bars are respectively for total, linear, and circular polarisations. The solid curves of the corresponding colour are the model fitting excluding data in the grey region (see Methods). The oscillation phase difference ( $\Delta\Phi$ ) between the linear and circular polarisation oscillations is denoted. (e) Linear polarisation angle as a function of the square of wavelength. The oscillation phase difference ( $\Delta\Psi$ , between the linear polarisation and polarisation angle) is denoted. All error bars in the figure are at the 95%-confidence level.

Figure 3: **Host-galaxy properties at optical and near-infrared wavelengths.** (a) Emission lines from the  $z = 0.098$  host galaxy in the LRIS (blue) and ESI (red) spectra. (b) The  $K'$ -band AO image of the barred-spiral host galaxy, with the indicated position of the FRB<sup>35</sup> shown as a cyan circle, the centroid of a  $z = 0.553$  background galaxy (Methods) marked by a yellow star, and the LRIS and ESI slit edges in blue and red solid lines, respectively.

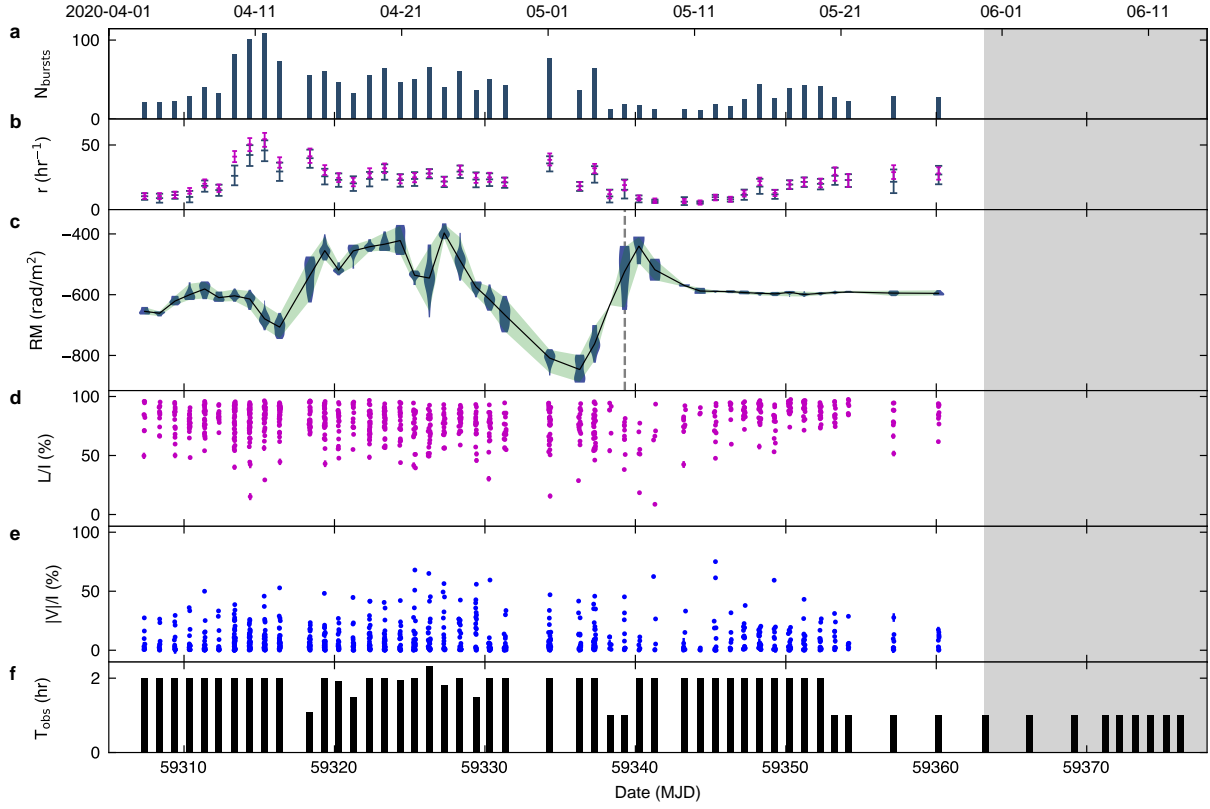


Figure 1: **Temporal variations of the physical parameters of FRB 20201124A.** (a) Daily number of bursts detected. (b) Weibull event rate (blue) and Poisson event rate (magenta). (c) Daily RM, where the violin symbol indicates the distribution function, the green shaded strips indicate the 95% upper and lower bounds, and the solid black curve is the median. Vertical dashed line indicates MJD 59339, where the largest RM fluctuation is noted. (d) and (e) Fractional linear and circular polarisations measured for each individual burst. (f) Observation length on each day. The grey shaded region on the right side of the plot shows the epoch when no burst was detected.

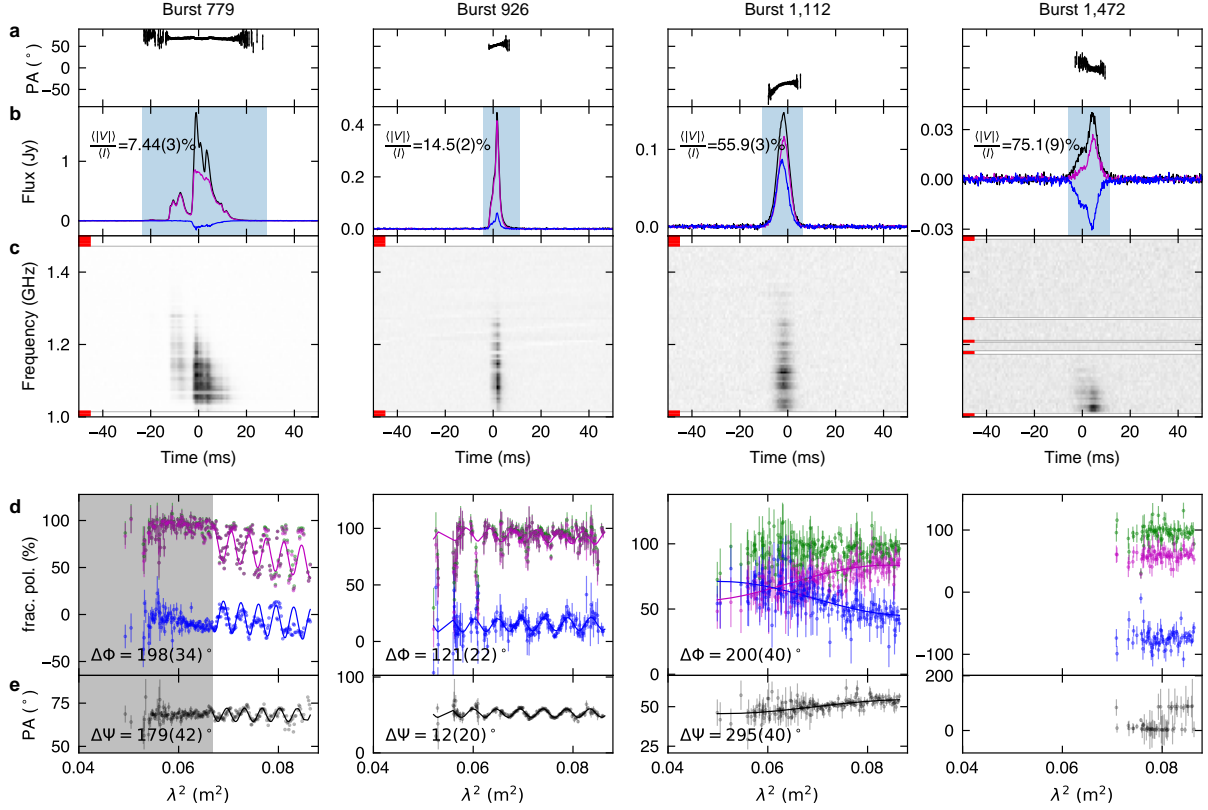


Figure 2: **Polarisation profiles, dynamic spectra, and frequency-dependent polarisation of selected bursts.** (a) PA curve. (b) Polarisation profile, where total intensity, linear, and circular polarisations normalised to the off-pulse noise of total intensity are in black, red, and blue curves, respectively. (c) Dynamic spectra of total intensity. The horizontal white strips and red markers represent frequency channels that have been removed owing to either radio-frequency interference (RFI) or band edges. (d) Fractional polarisation as a function of the square of wavelength, where green, magenta, and blue dots and error bars are respectively for total, linear, and circular polarisations. The solid curves of the corresponding colour are the model fitting excluding data in the grey region (see Methods). The oscillation phase difference ( $\Delta\Phi$ ) between the linear and circular polarisation oscillations is denoted. (e) Linear polarisation angle as a function of the square of wavelength. The oscillation phase difference ( $\Delta\Psi$ , between the linear polarisation and polarisation angle) is denoted. All error bars in the figure are at the 95%-confidence level.



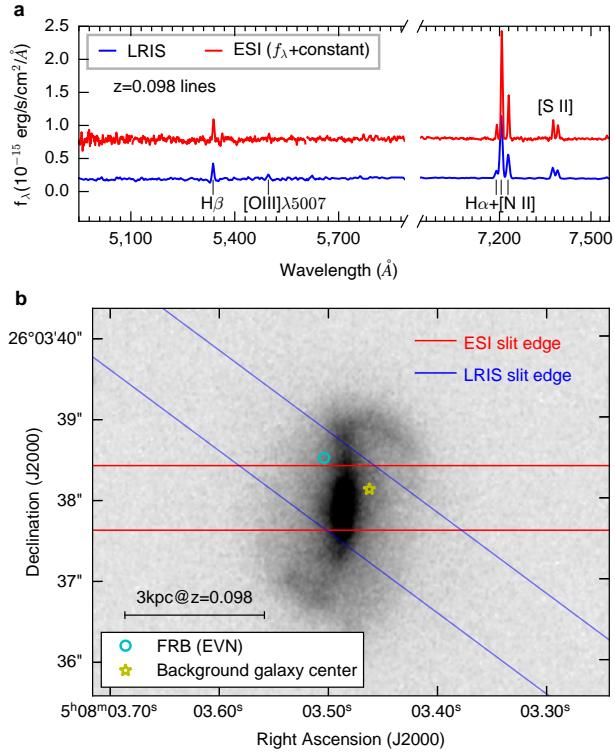


Figure 3: **Host-galaxy properties at optical and near-infrared wavelengths.** (a) Emission lines from the  $z = 0.098$  host galaxy in the LRIS (blue) and ESI (red) spectra. (b) The  $K'$ -band AO image of the barred-spiral host galaxy, with the indicated position of the FRB<sup>35</sup> shown as a cyan circle, the centroid of a  $z = 0.553$  background galaxy (Methods) marked by a yellow star, and the LRIS and ESI slit edges in blue and red solid lines, respectively.

## Methods

### Radio observations and burst detection

We carried out our observations using the 19-beam receiver of FAST on 2021 April 1. The 19-beam receiver spans from 1.0 GHz to 1.5 GHz with a system temperature of 20–25 K<sup>36</sup>. From 2021 April 1 to April 2, we performed a grid of 9 observations using all 19 beams around the position ( $\alpha = 05^{\text{h}}08^{\text{m}}$ ,  $\delta = +26^{\circ}11'$ ) reported by the CHIME/FRB team<sup>37</sup> and detected multiple bursts in 2 to 4 beams simultaneously. We then used the differential intensity in each beam to compute a refined location:  $\alpha = 05^{\text{h}}08^{\text{m}}03.50^{\text{s}}$ ,  $\delta = +26^{\circ}03'37.80''$ <sup>38</sup>. From May 15 onward, observations were carried out by pointing the FAST central beam at the much more precise European Very Long Baseline Interferometry Network (EVN) position<sup>35</sup> ( $\alpha = 05^{\text{h}}08^{\text{m}}03.507^{\text{s}}$ ,  $\delta = +26^{\circ}03'38.50''$ ). The epochs and durations of all observations are shown in Figure 1. The data of April 1 and 2 were used only for localisation purposes<sup>38</sup>; they are excluded in other analyses in this paper, as the beam centre was misaligned with the source position. The data were recorded with a frequency resolution of 122.07 kHz and a temporal resolution of 49.152  $\mu\text{s}$  or 196.608  $\mu\text{s}$ . The FAST receiver uses the dual-polarisation linear polarisation feed<sup>36</sup>, with which the 4-channel Stokes intensity was measured. Before and after each observation session, we recorded a 1 minute noise diode signal for the polarisation calibration.

We used the software TRANSIENTX (<https://github.com/ypmen/TransientX>) to perform the off-line burst searches. The data were dedispersed in the range of 380–440  $\text{cm}^{-3}$  pc with a step of 0.1  $\text{cm}^{-3}$  pc and the burst width was searched with a boxcar filter, of which the filter width ranges from 0.1 ms to 100 ms. After candidate plots were formed, we visually inspected all 3364 candidates with  $S/N \geq 7$ <sup>39</sup>. A total of 1863 bursts were detected in our observations; the detected number of bursts for each observation session is plotted in Figure 1. We also verified the search results using the software BEAR<sup>40</sup>. No difference can be found for bursts with  $S/N \geq 7$ .

### Event-rate evolution and the quenching

We adopted the Weibull distribution<sup>41</sup> to describe the probability density of time intervals between bursts. The Weibull distribution of time interval  $\delta$  is

$$W(\delta|k, r) = k\delta^{-1}[\delta r\Gamma(1 + 1/k)]^k e^{-[\delta r\Gamma(1+1/k)]^k}, \quad (1)$$

where the function  $\Gamma(x) \equiv \int_0^\infty t^{x-1}e^{-t}dt$ ;  $r$  and  $k$  are the event rate and shape parameter, respectively. The statistical inferences were carried out using the Bayesian method<sup>41</sup> implemented with the software package MULTINEST<sup>42</sup>. The inferred daily event rate and shape parameter are shown

in Figure 1 and Extended Data Figure 1. The inferred average event rate and shape parameter are  $r = 21 \pm 2 \text{ hr}^{-1}$  and  $k = 0.60 \pm 0.02$  for a 95% confidence level, where  $k < 1$  indicates that the bursts tend to cluster together. The Poisson rate, implicitly assuming no temporal correlation, is computed by fixing  $k = 1$ . As shown in Figure 1, the two rates are consistent with each other within the 68% confidence-level error. The event rate is not constant as the reduced  $\chi^2$ , assuming constant rate, for all 45 measurements are 6.3 and 12.0 (the corresponding  $P$ -values are  $10^{-35}$  and  $10^{-83}$ ) for the Weibull and Poisson cases, respectively. On May 29 (MJD 59363), the FRB source was quenched. No more bursts were detected with  $S/N \geq 7$  thereafter in 20 days with a total of 9 hr observations. The corresponding 95% confidence level upper limit of the event rate is  $r \leq 0.3 \text{ hr}^{-1}$ .

### Flux, fluence, and energy of bursts

We estimated the flux densities ( $S$ ) through the radiometer equation with a typical system temperature of 20 K and telescope gain  $G \approx 16 \text{ K Jy}^{-1}$  for FAST<sup>36</sup>. We calculate the flux density at a frequency resolution of 7.8125 MHz and a time resolution of 196.608  $\mu\text{s}$ . The dominant uncertainty ( $\sim 20\%$ ) in flux-density estimation comes from the temporal variation of system temperature<sup>36</sup>. The average flux density is derived from the Gaussian fitting method<sup>43</sup>. Since the average flux will depend on the definition of “signal bandwidth”, we choose the  $3\sigma$  width from the Gaussian fitting as our signal bandwidth. The average burst fluence ( $F$ ) is computed by integrating the average burst flux with respect to time, and the equivalent width  $W_{\text{eq}}$  is computed by dividing the fluence by the burst peak flux. The measured distributions  $F$  and  $W_{\text{eq}}$  are shown in Extended Data Figure 2. The average and the RMS deviation of  $W_{\text{eq}}$  are 7.6 ms and 3.3 ms, respectively, while the average  $F$  and its RMS fluctuation are 0.5 Jy ms and 1.0 Jy ms.

The sample completeness was determined with the following method. We simulated 10,000 mock bursts with Gaussian profile and bandpass matching the detected distributions. We then randomly injected the mock bursts into the original FAST data when no FRB was detected. The mock burst injected data are then fed to our burst-searching pipeline to compute the detection rate. The procedure shows that the fluence threshold achieving the 95% detection probability with  $S/N \geq 7$  is 53 mJy ms.

The isotropic burst energy  $E$  was calculated by integrating over the  $4\pi$  solid angle and the signal bandwidth,  $E = 4\pi D_L^2 (1+z)^{-1} \int F \text{ dBW}$ , where  $D_L = 453.3 \pm 0.1 \text{ Mpc}$  is the luminosity distance<sup>26</sup>, and  $F$  is the fluence. The energy inference is little affected by the choice of BW, as it is integrated. We evaluate the systematics by comparing the energy measured from integrating  $2\sigma$  and  $3\sigma$  Gaussian-fitting BW. The difference ( $\Delta E/E \leq 10\%$ ) is smaller than the 20% uncertainty

in the system temperature.

The histogram of burst energies and the cumulative distribution function (CDF) of the burst energy are shown in Extended Data Figure 2. We note that the CDF of burst energy is better fitted by a broken power law rather than by a single power law; i.e., we use

$$N(\geq E) \propto \begin{cases} E^{-\gamma_1} & \text{for } E < E_0, \\ E^{-\gamma_2} & \text{for } E \geq E_0, \end{cases} \quad (2)$$

where  $\gamma_1$  and  $\gamma_2$  are the power-law indices, and  $E_0$  is the turning-over energy. The inferred parameters for the broken power law model are  $\gamma_1 = 0.36 \pm 0.02 \pm 0.02$ ,  $\gamma_2 = 1.5 \pm 0.1 \pm 0.1$ , and  $E_0 = 1.1 \pm 0.1 \pm 0.1 \times 10^{38}$  erg. Here, the former uncertainty is for the 95% confidence-level statistical error, while the later one comes from the 20%  $T_{\text{sys}}$  variation. The natural logarithmic Bayesian factor ( $\ln \mathcal{B}$ ) of the broken power law model over the single power law model is 1275, which indicates a strong preference for the former. Our measured power-law index at the higher-energy end ( $\gamma_2$ ) is close to that of FRB 20121102A<sup>14</sup> (i.e.,  $\gamma \sim 1.4$  for  $E > 3 \times 10^{38}$  erg), and it is also close to the power-law index ( $\gamma \approx 1.3$ ) of the bright bursts of FRB 20180916B detected by CHIME<sup>43</sup>. The power-law index at the lower-energy end ( $\gamma_1$ ) is shallower than that measured in FRB 20121102A<sup>14</sup> with  $\gamma = 0.61 \pm 0.04$  for  $4 \times 10^{36} < E < 3 \times 10^{38}$ . We tested the effects of Gaussian fitting BW on  $\gamma$  by comparing the value derived using  $2\sigma$  and  $3\sigma$  BW values, where  $\delta\gamma_1 = 0.02$  and  $\delta\gamma_2 = 0.06$  are comparable to the systematics of  $T_{\text{sys}}$  variation. We searched for the corresponding high-energy transients in both *Fermi* and *Insight-HXMT/GECAM* data<sup>44,45</sup>, and the null detection places loose bounds that the ratio between the luminosity in radio and  $\gamma$ -ray bands, i.e.  $L_{\text{radio}}/L_{\gamma} \geq 1.4 \times 10^{-7}$  (8–200 keV) and  $\geq 6.3 \times 10^{-7}$  (200–3,000 keV).

### Waiting time between the bursts

The burst times of arrival (TOAs) were measured from the centroid of the best-matched boxcar filter<sup>40</sup>. We then converted the site arrival times to the barycentric coordinate time at the reference frequency of 1500 MHz using the software package TEMPO2<sup>46</sup>. The waiting times ( $\Delta T_{\text{wait}}$ ) were calculated by subtracting two adjacent barycentric TOAs. The distribution of the waiting time is shown in Extended Data Figure 3. We modeled it using the superposition of three log-normal distributions, where the best-fitting curve to the histogram is in Extended Data Figure 3. The waiting-time distribution shows local maxima at 39 ms, 45.1 s, and 162.3 s. We note that a superposition of two log-normal distributions is insufficient to describe the data (Extended Data Figure 3), which can be verified by the large value of natural logarithmic Bayesian factor ( $\ln \mathcal{B} = 35$ ) of the three-component model over the two-component model. The multimodal distribution of waiting times is

similar to the case of FRB 20121102A<sup>14</sup>, except that the shortest waiting-time population (39 ms) is one order of magnitude longer than that of FRB 20121102A (3.4 ms).

### Dispersion measure (DM)

We used the Fourier-domain method to measure the dispersion measure (DM), where the DM is measured by maximising the time derivative of “intensity” computed only with the Fourier phase ([https://www.github.com/DanieleMichilli/DM\\_phase](https://www.github.com/DanieleMichilli/DM_phase)). The DM values as a function of time are collected in Extended Data Figure 1. The mean value is  $413.2 \text{ cm}^{-3} \text{ pc}$  and the RMS deviation is  $2.0 \text{ cm}^{-3} \text{ pc}$ . A linear fit shows no obvious trend in DM with a 95% confidence-level upper limit of  $|\text{dDM}/\text{dt}| \leq 7 \times 10^{-3} \text{ cm}^{-3} \text{ pc day}^{-1}$ , while there is a peak-to-peak fluctuation of  $\sim 10 \text{ cm}^{-3} \text{ pc}$  in the burst-to-burst DM.

The measured DM agrees with the theoretical expectation. The observed DM is  $\sim 413 \text{ cm}^{-3} \text{ pc}$ . The Galactic interstellar medium (ISM) contribution is  $\text{DM}_{\text{MW}} \approx 140 \text{ cm}^{-3} \text{ pc}$  or  $\text{DM}_{\text{MW}} \approx 200 \text{ cm}^{-3} \text{ pc}$  according to the NE2001 model<sup>47</sup> and the YMW16 model<sup>48</sup>, respectively. Considering a Galactic-halo contribution of  $\sim 30 \text{ cm}^{-3} \text{ pc}$ <sup>49</sup>, the total Galactic contribution is in the range  $170\text{--}230 \text{ cm}^{-3} \text{ pc}$ . The rest of all the extragalactic DM contributions would thus be  $183\text{--}243 \text{ cm}^{-3} \text{ pc}$ . Further accounting for the intergalactic medium contribution of  $\text{DM}_{\text{IGM}} \approx 80 \text{ cm}^{-3} \text{ pc}$  at  $z = 0.09795$ <sup>50</sup>, the FRB host-galaxy DM contribution should be in the range  $103\text{--}163 \text{ cm}^{-3} \text{ pc}$ . This value agrees with the modeling of the host galaxy using the DM template technique<sup>51</sup>, which predicted that the 68%-confidence-level range of the host-galaxy DM is  $10 \leq \text{DM}_{\text{host}}/(1+z) \leq 300 \text{ cm}^{-3} \text{ pc}$ , where the host-galaxy  $\text{H}\alpha$  luminosity  $L_{\text{H}\alpha} = 7 \times 10^{41} \text{ erg s}^{-1}$  and the effective radius  $R_e = 1.5 \text{ kpc}$  are from our optical observations (see the optical observation section in Methods).

### Polarisation properties

Our polarisation data are calibrated with the single-axis model using the software package PSRCHIVE<sup>52</sup>, where both the differential gain and phase between the two polarisation channels are calibrated using noise diode signal injected in the feed. The polarisation fidelity and calibration scheme have been described and tested in previous work<sup>17,36</sup>.

We measure the RM for high-quality bursts only with  $S/N \geq 30$  (1103 in total) using the  $Q - U$  fitting method<sup>53</sup>. We corrected the ionosphere contribution with values computed from the software package IONFR<sup>54</sup>, where the maximal ionosphere RM correction is  $3 \text{ rad m}^{-2}$ . The RM in the FRB’s source rest frame<sup>55,56</sup> is  $\text{RM}_{\text{host}} = (1+z)^2(\text{RM}_{\text{obs}} - \text{RM}_{\text{Gal}}) = -380 \text{ rad m}^{-2}$  to

$-1010 \text{ rad m}^{-2}$ .

We can exclude a few common origins for the RM variation. (1) The RM variation cannot be explained with the RM contribution in the MW, which is  $-51(5) \text{ rad m}^{-2}$  along the direction of FRB 20201124A; the maximal variation is a few tens of radians per square meter within a  $2^\circ$  field of view<sup>57</sup>. (2) The RM variation is not caused by instrumental artifacts. In polarisation studies, we have excluded the data of April 1 and 2, where the observations were carried out with off-axis illumination. The FAST polarimetry stability has been checked<sup>17</sup> to show that the RM measurement is stable with  $\Delta\text{RM} \leq 0.2 \text{ rad m}^{-2}$ . We also checked if saturation or nonlinearity affected our polarimetry. The digital sampling and data recording is done with an 8-bit sampling scheme at FAST. We tested the nonlinearity by comparing the differences in results between including and removing the data above 250 (the maximal digital value is 255 for an 8-bit system); the differences are tiny. (3) RM variation is not from the apparent RM variation across the phase of a burst as found in pulsars<sup>58</sup> and in FRBs<sup>59</sup>. We find that the maximum amplitude of RM variations within single bursts for FRB 20201124A is at the level of  $15 \text{ rad m}^{-2}$  (examples are shown in Extended Data Figure 4), which is too small to explain the RM variation of FRB 20201124A at the level of  $\sim 500 \text{ rad m}^{-2}$ . (4) RM variation is not caused by the intrinsic frequency evolution of individual bursts, as the PA rotation matches the cold plasma Faraday rotation relation. We relaxed the power-law index of wavelength in  $Q - U$  fitting and also fit for the RM index  $\beta$  using the model  $\Delta\Psi = \text{RM} \lambda^\beta$ . One expects  $\beta = 2$  if the cold plasma Faraday rotation model can be applied, while the index  $\beta$  would not necessarily equal 2 if the apparent RM is caused by intrinsic profile evolution. As shown in Extended Data Figure 5, we found that for 57% of the bursts (631 out of 1103 bursts), the deviations of measured RM index values are within  $1\sigma$  error bars. Visual inspection revealed that the  $\beta \neq 2$  deviation was mainly caused by overlapping of multiple components in the dynamic spectrum. The detected trend of RM variation is hardly affected by the  $\beta \neq 2$  deviation as shown in Extended Data Figure 5. To further reduce the profile-evolution effects, only the measurements with RM index within  $1\sigma$  of  $\beta = 2$  are included in Figure 1.

Considering the 10-day timescale of RM variation, we expect that the major RM variation comes from the FRB local environment, over a distance scale of  $\Delta X \approx 0.6 \text{ au} (\tau/10 \text{ day})(v/100 \text{ km s}^{-1})$ , where we normalised velocity to the typical value of binary motion or proper motion of neutron stars. We can derive a bound on the parallel magnetic field by using the constraint induced by free-free absorption at such a small distance scale. The detection of FRB emission requires that the free-free absorption optical depth should be smaller than unity<sup>60,61</sup>, which means that the local DM contributing to the RM variation meets

$$\Delta\text{DM} < 4\eta \left( \frac{T}{10^4} \right)^{0.7} \left( \frac{\nu}{\text{GHz}} \right)^{1.1} \left( \frac{\Delta X}{\text{au}} \right), \quad (3)$$

where we converted the DM to EM via the filling factor  $\eta \equiv \frac{\Delta\text{DM}^2}{\Delta X_{\text{EM}}} \leq 1$ . One finds

$$\langle B_{\parallel} \rangle = 1.23 \mu\text{G} \frac{\Delta\text{RM}}{\Delta\text{DM}} > 0.2 \text{ mG} \eta^{-1} \left( \frac{\Delta\text{RM}}{500 \text{ rad m}^{-2}} \right) \left( \frac{T}{10^4} \right)^{-0.7} \left( \frac{\nu}{\text{GHz}} \right)^{-1.1} \left( \frac{\Delta X}{\text{au}} \right)^{-1}. \quad (4)$$

Here RM is defined in the source rest frame. Such a mG-level lower bound of the magnetic field was also reported for FRB 20121102A<sup>16,62</sup> based on the host-galaxy DM estimation.

For 41 of the total 1863 bursts, we have discovered oscillations of fractional circular/linear polarisation ( $\Pi_V \equiv V/I$ ,  $\Pi_L \equiv L/I$ ), and linear PA. The oscillation can be characterised with periodicity in the square of wavelength, and we use the Lomb-Scargle periodogram<sup>63</sup> to find such features. A  $\chi^2$  fitting to the following model simultaneously for circular and linear polarisation intensities is used to infer the oscillation parameters:

$$L = I \left[ \Pi_{L0} + \dot{\Pi}_L \lambda^2 + A \sin(\omega_{\lambda^2} \lambda^2 + \phi_L) \right], \quad (5)$$

$$V = I \left[ \Pi_{V0} + \dot{\Pi}_V \lambda^2 + A \sin(\omega_{\lambda^2} \lambda^2 + \phi_V) \right], \quad (6)$$

$$Q = L \cos \left[ \text{PA}_0 + A_{\text{PA}} \cos(\omega_{\lambda^2} \lambda^2 + \phi_{\text{PA}}) \right], \quad (7)$$

$$U = L \sin \left[ \text{PA}_0 + A_{\text{PA}} \cos(\omega_{\lambda^2} \lambda^2 + \phi_{\text{PA}}) \right], \quad (8)$$

where the parameters  $\Pi_{L0}$ ,  $\dot{\Pi}_L$ ,  $\Pi_{V0}$ , and  $\dot{\Pi}_V$  are the average values and the slopes of the fractional linear and circular polarisation,  $A$  is the amplitude of oscillation in the fractional polarisation,  $\text{PA}_0$  is the mean PA, and  $A_{\text{PA}}$  is the amplitude of the oscillation in PA. A common angular frequency of oscillation ( $\omega_{\lambda^2}$ ) is assumed for  $\Pi_V, \Pi_L$  and PA. The  $\phi_L$ ,  $\phi_V$ , and  $\phi_{\text{PA}}$  are oscillation phases. The best-fitting conjugate frequencies of bursts 779 and 926 are  $\omega_{\lambda^2} = 2400 \pm 30 \text{ rad m}^{-2}$  and  $1800 \pm 10 \text{ rad m}^{-2}$ . In the framework of mild polarisation absorption or Faraday conversion, one has  $|\text{RM}'| = \omega_{\lambda^2}/2$ , which is the Faraday rotation accumulated from the FRB, along the line of sight, up to the position where the absorption or conversion occurs:  $\text{RM}' = 1200 \pm 15 \text{ rad m}^{-2}$ ,  $900 \pm 5 \text{ rad m}^{-2}$ , respectively. We note that the total observed RM is of the same order of magnitude, which indicates that a significant amount of RM comes from the vicinity of the FRB source, where, at the same time, Faraday conversion or synchrotron absorption is still important<sup>64,65</sup>, i.e. a cold and a relativistic plasma coexist.

We plot the best-fit curves against the data in Figure 2, where we convert the model to fractional polarisation for better visualisation. The best-fit phase differences between the linear and circular oscillations are given in panel (d) of Figure 2. For burst 779, the oscillations of  $\Pi_V$  and  $\Pi_L$  decrease significantly above 1160 MHz ( $\lambda^2 \leq 0.067 \text{ m}^2$  as indicated by the shaded area in Figure 2), where the best-fit amplitudes of oscillation below and above 1160 MHz are  $0.16 \pm 0.01$  and  $0.008 \pm 0.005$ , respectively. Such frequency-dependent oscillation can be explained with the

characteristic frequency of a uniformly magnetised plasma<sup>65</sup> that the plasma effects are important when wave frequency below the characteristic frequency, i.e.  $f \leq 0.04 \text{ GHz } (B/\text{G})\gamma^2$ , with  $\gamma$  the electron kinetic Lorentz factor. In the polarisation-dependent radiative transfer framework, the constraint for magnetic field becomes  $B \geq 3 \text{ G } (f/1.1\text{GHz})(\gamma/10)^{-2}$ .

We checked the power-law index of oscillation with respect to  $\lambda$  by replacing terms of  $\omega_{\lambda^2}\lambda^2$  in Eq. (5) and (6) to a generalised form of  $\omega_{\lambda^{2k}}\lambda^{2k}$  and fit the index  $k$  simultaneously. For bursts 779 and 926, we had  $k = 0.998 \pm 0.005$  and  $1.0 \pm 0.1$ , which verifies the  $\lambda^2$ -dependent oscillation of polarisation.

Besides Faraday conversion, polarisation-dependent scintillation can also induce such  $\lambda^2$ -dependent oscillations<sup>66</sup>, if the number of slits on the scintillation screen is limited. However, special conditions are required in this model to reproduce the observation. First, polarisation-dependent absorption is still required to induce oscillation in total polarisation  $\Pi_{\text{P}}$ . Second, contrived fine tuning is required to achieve a 40%  $\Pi_{\text{V}}$  variation for a  $< 10^\circ$  PA change as seen in burst 779. Also, an extra mechanism is needed to cease the polarisation oscillations above 1160 MHz for burst 779.

We note that not all bursts with the measured nonzero  $\Pi_{\text{V}}$  show the above oscillatory behaviour. Some bursts exhibit slow variations with opposite phases of  $\Pi_{\text{V}}$  and  $\Pi_{\text{L}}$ , such as burst 1112 in Figure 2. The variation may come from Faraday conversion or an intrinsic radiation mechanism of FRBs. Interestingly, the burst with the highest  $\Pi_{\text{V}}$  in our sample (burst 1472 in Figure 2) shows no significant oscillation. Therefore, on top of Faraday conversion, an alternative, intrinsic radiation mechanism may be required to generate circular polarisation.

## Keck optical and near-infrared observations

We obtained Keck I low- and high-dispersion spectra with the Low Resolution Imaging Spectrometer (LRIS)<sup>67,68</sup> and the Echellette Spectrograph Imager (ESI)<sup>69</sup>, respectively. The LRIS spectra were taken with a slit width of  $1.0''$  at PA =  $53.4^\circ$ , and there were  $750 + 920$  s and  $2 \times 750$  s exposures on the blue and red sides, respectively. LRIS has an atmospheric dispersion corrector. The data were reduced using LPipe<sup>70</sup>, and the fluxes were scaled to match Pan-STARRS1<sup>71</sup> *griz* photometry. Galactic extinction corrections<sup>72,73</sup> were applied with  $R_V = 3.1$  and  $E(B - V)_{\text{MW}} = 0.652$  mag. We took  $8 \times 320$  s exposures with ESI in the cross-dispersed echelle mode with resolving power  $R \approx 10,000$  and a slit width of  $1.0''$  at the parallactic angle<sup>74</sup> of  $87^\circ$ . They were reduced with ESIRedux (<https://www2.keck.hawaii.edu/inst/esi/ESIRedux/index.html>), with only relative-flux calibration performed.



The LRIS imaging consisted of  $4 \times 180$  s exposures in the  $g$  band and  $2 \times 180$  s in the  $i$  band. They were reduced following standard procedures of bias subtraction, flat fielding, and coadding.

We obtained  $4 \times 120$  s near-infrared  $K'$ -band images (dithered by  $3\text{--}4''$  between exposures) with the NIRC2 camera ( $0.04'' \text{ pixel}^{-1}$  scale and  $40''$  field) via the Keck II laser-guide-star AO system<sup>75</sup>. An  $R = 15.9$  mag star  $36''$  NW of the FRB host served as the tip-tilt reference star. The images were reduced following a standard iterative procedure implemented in an IDL package (<https://github.com/fuhaiastro/nirc2>), and the final combined image reaches a full width at half-maximum intensity (FWHM) resolution of  $0.12''$ . The astrometry is calibrated using five stars in the field to the *Gaia* reference frame (Gaia-CRF2<sup>76</sup>), which is tied to the International Celestial Reference System (ICRF) reference system using accurate VLBI positions of quasars at sub-mas precision.

## Properties of the host galaxy

**Star-formation rate and gas-phase metallicity:** We use the emission lines detected in the high- $S/N$  LRIS spectrum to measure the redshift ( $z = 0.09795 \pm 0.00003$ ), infer the star-formation rate (SFR), and determine the gas-phase metallicity of the galaxy. We measure line fluxes of  $\text{H}\alpha$ ,  $[\text{N II}] \lambda 6548$ ,  $[\text{N II}] \lambda 6583$ ,  $[\text{O III}] \lambda 5007$ ,  $[\text{O II}] \lambda 3726, 3729$ , and  $[\text{S II}] \lambda 6716, 6731$  by fitting single-Gaussian profiles; for  $\text{H}\beta$ , we add an additional Lorentzian component to account for stellar absorption.

We use the  $\text{H}\alpha$  luminosity  $L(\text{H}\alpha)$  to estimate the SFR. The internal extinction of the galaxy is estimated with the Balmer decrement by adopting  $(\text{H}\alpha/\text{H}\beta)_{\text{theory}} = 2.86$  for Case B recombination and using the Calzetti et al.<sup>77</sup> reddening curve; we obtain  $E(B - V) = 0.43 \pm 0.04$  mag and thus  $A_{\lambda}(\text{H}\alpha) = 1.27 \pm 0.12$  mag, yielding  $L(\text{H}\alpha) = (6.9 \pm 0.7) \times 10^{41} \text{ erg s}^{-1}$ , which translates to  $\text{SFR} = 3.4 \pm 0.3 M_{\odot} \text{ yr}^{-1}$ <sup>78</sup>. Our SFR estimate is higher than previous  $L(\text{H}\alpha)$ -based measurements,  $\sim 2.1 M_{\odot} \text{ yr}^{-1}$ <sup>10</sup>,  $\sim 1.7 M_{\odot} \text{ yr}^{-1}$ <sup>11</sup>, and  $2.3 \pm 0.4 M_{\odot} \text{ yr}^{-1}$ <sup>12</sup>, while it is lower than those derived from spectral energy distribution (SED) fitting ( $\sim 4.3 M_{\odot} \text{ yr}^{-1}$ <sup>10</sup>) and radio data ( $\sim 7 M_{\odot} \text{ yr}^{-1}$ <sup>11</sup> and  $\sim 10 M_{\odot} \text{ yr}^{-1}$ <sup>12</sup>). Adopting a stellar mass  $M_{*} = (2.5 \pm 0.7) \times 10^{10} M_{\odot}$  for the galaxy from averaging two existing results<sup>10,11</sup>, the specific SFR is  $\log(\text{sSFR}/\text{yr}^{-1}) = -9.86 \pm 0.11$ . We also cross-check it by estimating sSFR using the equivalent width (EW) of  $\text{H}\alpha$ ,  $\text{EW}(\text{H}\alpha) = 48 \text{ \AA}$  and obtain  $\log(\text{sSFR}/\text{yr}^{-1}) = -9.65 \pm 0.19$ <sup>79</sup>; it is higher than our  $L(\text{H}\alpha)$ -based estimate by  $\sim 1 \sigma$ .

We infer the gas-phase metallicity ( $Z$ ) by applying the Inferring metallicities ( $Z$ ) and Ionization parameters ( $q$ ) (IZI) photoionisation model<sup>80,81</sup> to the fluxes of all the above-mentioned emission lines, yielding a best-fit oxygen abundance of  $12 + \log(\text{O}/\text{H}) = 9.07_{-0.04}^{+0.03}$ , in agreement

with a previous estimate<sup>10</sup> ( $12 + \log(\text{O}/\text{H}) = 9.03_{-0.24}^{+0.15}$ ) using the “O3N2” method.

**Morphology and kinematics:** The left and middle subpanels of Extended Data Figure 6(a) show the LRIS  $i$ -band image and the NIRC2  $K'$ -band AO image, respectively. The AO image with  $\text{FWHM} = 0.12''$  enables us to resolve the bar and spiral features of the galaxy, which is not possible with natural seeing. We used GALFIT<sup>82</sup> to model the host galaxy in the NIRC2 image with a single-component model composed of a Sérsic profile in the radial direction and a generalised ellipse function in the azimuthal direction. We obtain the best-fit effective radius  $R_e = 1.5$  kpc and axis ratio  $b/a = 0.62$ , which suggests  $\cos(i) = 0.6$  (where  $i$  is disc inclination angle)<sup>83,84</sup>.

After subtracting the disc component, the galaxy bar and spiral features can be clearly seen in the residual NIRC2 image shown in the right-most subpanel of Extended Data Figure 6(a). We measure the centroid of the galaxy bar by fitting a two-dimensional (2D) Gaussian model and obtain refined J2000 coordinates of the galaxy centre ( $\text{RA} = 05^{\text{h}}08^{\text{m}}03.4896^{\text{s}}$ ,  $\text{Dec} = +26^{\circ}03'37.869''$ ). The FRB is  $0.239 \pm 0.013''$  and  $0.636 \pm 0.007''$  to the east and north of the galaxy centre, respectively. The uncertainties are estimated by adding the localisation uncertainties from EVN ( $\Delta\text{RA}_{\text{EVN}} = 4.5$  mas and  $\Delta\text{Dec}_{\text{EVN}} = 3.6$  mas<sup>35</sup>) and optical observations ( $\Delta\text{RA}_{\text{opt}} = 12.0$  mas and  $\Delta\text{Dec}_{\text{opt}} = 6.5$  mas) in quadrature. The error budget of optical astrometry is dominated by the uncertainties from the Keck-*Gaia* frame transformation, whereas the centroiding errors in Keck (2 mas) and *Gaia* (from a fraction of 1 mas to  $\sim 2$  mas for the five reference stars) are relatively minor.

The object’s projected position is on the disc, although it does not seem to coincide with any other visible structures. We measure the one-dimensional intensity profile of a chord slicing through the FRB position and perpendicular to the major axis of the bar on the NIR2 image. We find that it is well described by a model of concentric double Gaussian functions with the broader ( $\sigma = 511$  mas) and narrower ( $\sigma = 96$  mas) Gaussians describing the disc and the bar contributions, respectively. We subtract the broader Gaussian (i.e., the disc contribution) and find that at the position of the FRB, which is  $260 \pm 13$  mas from the bar centre, its light has only 7% of the peak bar intensity, which is very small.

As shown in Extended Data Figure 6(b), the  $\text{H}\alpha$  line in the ESI spectrum has a double-peaked profile with a peak-to-peak separation of  $\sim 100$   $\text{km s}^{-1}$ , which may be due to disc rotation; however, since the ESI slit was oriented along the minor axis of the galaxy, it may alternatively be caused by gas outflow. We study the disc rotation with LRIS, for which the slit was oriented  $60^\circ$  with respect to the major axis. As shown in the left subpanels of Extended Data Figure 6(c), the wavelength centroids of  $\text{H}\alpha$  emission vary along the LRIS slit direction. We extract  $\text{H}\alpha$  lines with

a step size of 3 pixels ( $0.4''$ ) along the slit direction, and we measure their projected galactocentric distance ( $r_{\perp}$ ) and line-of-sight velocities ( $v$ ) to the continuum centre shown as the black dots in the right subpanel of Extended Data Figure 6(c). Then we fit the data using a simple rotational disc model, in which velocity scales linearly with galactocentric distance  $r$  for  $r < r_{\text{break}}$  (the velocity zero point is a free parameter) and stays constant at  $v_{\text{ROT}}$  for  $r > r_{\text{break}}$ . The best-fit model, which is shown as the red line in the right subpanel of Extended Data Figure 6(c), has the deprojected rotation velocity  $v_{\text{ROT}} = 139 \pm 19 \text{ km s}^{-1}$  and  $r_{\text{break}} = 3.0 \pm 0.5 \text{ kpc}$ . Our  $v_{\text{ROT}}$  estimate suggests a galaxy stellar mass  $M_* \approx 2 \times 10^{10} M_{\odot}$  using the Tully-Fisher relation<sup>84,85</sup>. This is consistent with our adopted value  $M_* = (2.5 \pm 0.7) \times 10^{10} M_{\odot}$  from averaging two previous estimates<sup>10,11</sup>.

### Background galaxy

Fong et al.<sup>10</sup> tentatively identified a background galaxy with the possible detection of  $\text{H}\beta$  and  $[\text{O III}]$  emission lines at  $z = 0.5531$ . Our spectra allow its firm identification and study of its properties. We detect  $\text{H}\alpha$ ,  $\text{H}\beta$ , and  $[\text{O III}] \lambda\lambda 4959, 5007$  emission lines at  $z = 0.5534 \pm 0.0001$  in the LRIS (blue) and ESI (cyan) spectra (see Extended Data Figure 7(c)). Owing to the nondetection of  $[\text{N II}]$  (or  $[\text{O II}]$ ), we cannot distinguish between a star-forming galaxy and an active galactic nucleus (AGN) in the Baldwin-Phillips-Terlevich (BPT) diagram (see Extended Data Figure 7(a)). The  $[\text{O III}] \lambda 5007$  line is resolved by ESI with a velocity dispersion  $\sigma_{[\text{O III}] \lambda 5007} = 27.6 \pm 2.6 \text{ km s}^{-1}$ ; such a low velocity dispersion favours that it is a star-forming galaxy<sup>86</sup>. Using IZI, we find that its gas-phase metallicity  $12 + \log(\text{O}/\text{H}) = 8.29_{-0.28}^{+0.26}$  and  $E(B - V) = 0.27_{-0.13}^{+0.12} \text{ mag}$ . The extinction-corrected  $\text{H}\alpha$  luminosity is  $L(\text{H}\alpha) = 1.14_{-0.38}^{+0.51} \times 10^{42} \text{ erg s}^{-1}$ , which yields  $\text{SFR} = 5.7_{-1.9}^{+2.5} M_{\odot} \text{ yr}^{-1}$ .

The centres of  $[\text{O III}] \lambda 5007$  emission from the background galaxy are offset from the centre of the continuum dominated by the host (foreground) galaxy in the 2D spectroscopic image. We measure the centroid of the background galaxy by using its  $[\text{O III}]$  emission line detected at two slit orientations, which are shown in Figure 3(b); it is  $0.29''$  west and  $0.22''$  north of foreground galaxy's centre. Owing to the large projected separation of 4.7 kpc, and inconsistency of the expected DM and scattering timescale<sup>87</sup>, it is unlikely that the background galaxy is the FRB host.

## Data availability

Raw data are available from the FAST data center, <http://fast.bao.ac.cn>. Owing to the large data volume, we encourage contacting the corresponding author for the data transfer. The directly related data that support the findings of this study can be found at the PSRPKU website, <https://psr.pku.edu.cn/index.php/publications/frb20201124a/> and Figshare website, <https://doi.org/10.6084/m9.figshare.19688854>.

## Code availability

PSRCHIVE (<http://psrchive.sourceforge.net>)

TRANSIENTX (<https://github.com/ypmen/TransientX>)

BEAR (<https://psr.pku.edu.cn/index.php/publications/frb180301/>)

**Acknowledgements** We are grateful to L. C. Ho, H. Gao, and R. Li for discussions. This work made use of data from the FAST. FAST is a Chinese national megascience facility, built and operated by the National Astronomical Observatories, Chinese Academy of Sciences. We acknowledge the use of public data from the Fermi Science Support Center (FSSC). This work is supported by National SKA Program of China (2020SKA0120100, 2020SKA0120200), Natural Science Foundation of China (12041304, 11873067, 11988101, 12041303, 11725313, 11725314, 11833003, 12003028, 12041306, 12103089, U2031209, U2038105, U1831207), National Program on Key Research and Development Project (2019YFA0405100, 2017YFA0402602, 2018YFA0404204, 2016YFA0400801), Key Research Program of the CAS (QYZDJ-SSW-SLH021), Natural Science Foundation of Jiangsu Province (BK20211000), Cultivation Project for FAST Scientific Payoff and Research Achievement of CAMS-CAS, the Strategic Priority Research Program on Space Science, the Chinese Academy of Sciences (grants XDA15360000, XDA15052700, XDB23040400), funding from the Max-Planck Partner Group, the science research grants from the China Manned Space Project (CMS-CSST-2021-B11, NO. CMS-CSST-2021-A11), and PKU development grant 7101502590. AVF's group at U.C. Berkeley is supported by the Christopher R. Redlich Fund, the Miller Institute for Basic Research in Science (in which AVF was a Miller Senior Fellow), and many individual donors. SD acknowledges support from the XPLOER PRIZE. BBZ is supported by Fundamental Research Funds for the Central Universities (14380046), and the Program for Innovative Talents, Entrepreneur in Jiangsu. Some of the data presented herein were obtained at the W.M. Keck Observatory, which is operated as a scientific partnership among the California Institute of Technology, the University of California, and NASA; the observatory was made possible by the financial support of the W.M. Keck Foundation. We thank the Keck staff for their help during the observing runs.

**Author Contributions** HX, JRN, and PC led the data analysis. KJL, WWZ, SD, and BZ coordinated

the observational campaign, cosupervised data analyses and interpretations, and led the paper writing. JCJ conducted the polarisation and RM measurements. BJW, JWX, CFZ, and KJL did the timing analysis, periodicity search, DM measurement, burst searching, and Faraday conversion measurement. YPM contributed to the searching software development. RNC, MZC, LFH, YXH, ZYL, ZXL, YHX, and JPY performed software testing. DJZ, YKZ, PW, YF, CHN, FYW, XFW, and SBZ contributed to radio data analysis. PC, SD, HF, AVF, EWP, TGB, SGD, PG, DS, AS, WKZ, and AE contributed to the optical observations and data reduction; AVF also edited the manuscript in detail. PC, SD, HF, and YL contributed to analysing and interpreting the optical data. PJ, HQG, JLH, JLH, HL, LQ, JHS, RY, YLY, DJY, and YZ aided with FAST observations. JLH, DL, MW, and NW helped with observation coordination. KJL, BZ, DZL, WYW, RXX, WL, YPY, WFY, ZGD, and RL provided theoretical discussions. CC, CKL, XQL, WXP, LMS, SX, SLX, JY, XY, QBY, BBZ, SNZ, and JHZ contributed to the high-energy observations and data analyses.

**Competing Interests** The authors declare no competing financial interests.

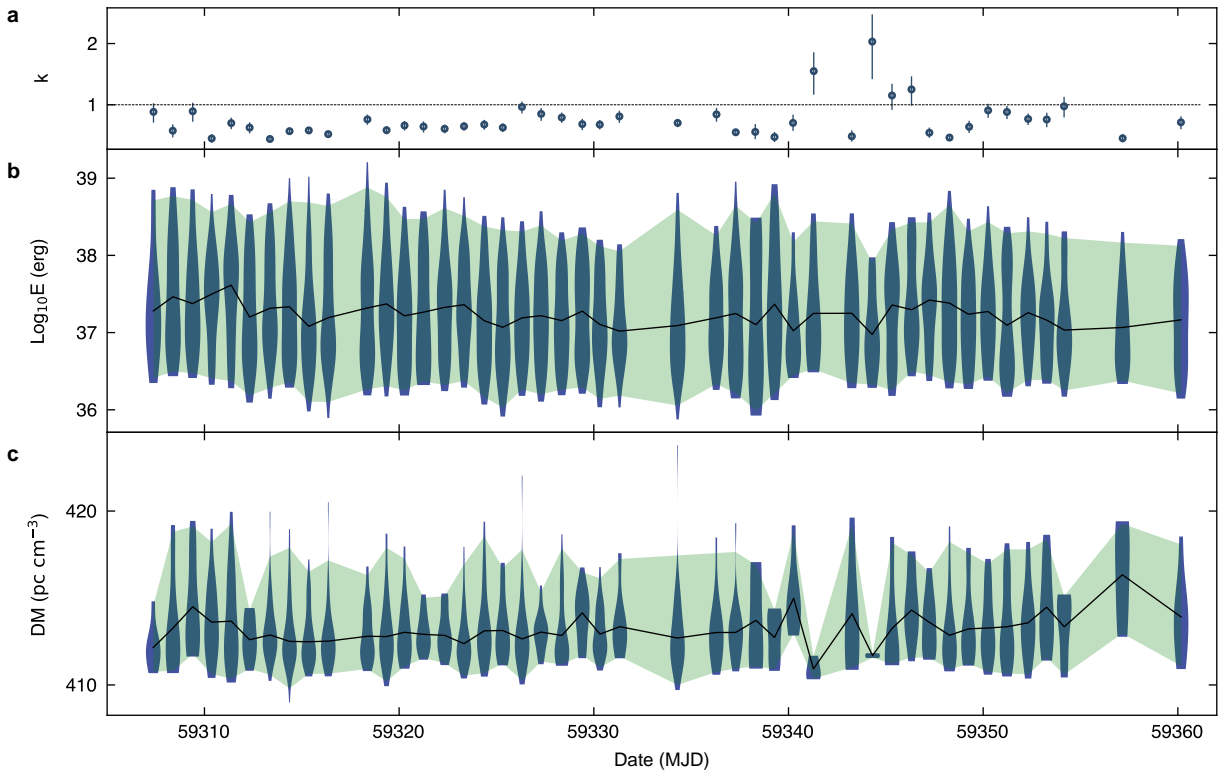
**Correspondence** Requests for materials should be addressed to the following:

K. J. Lee (E-mail: kjlee@pku.edu.cn)

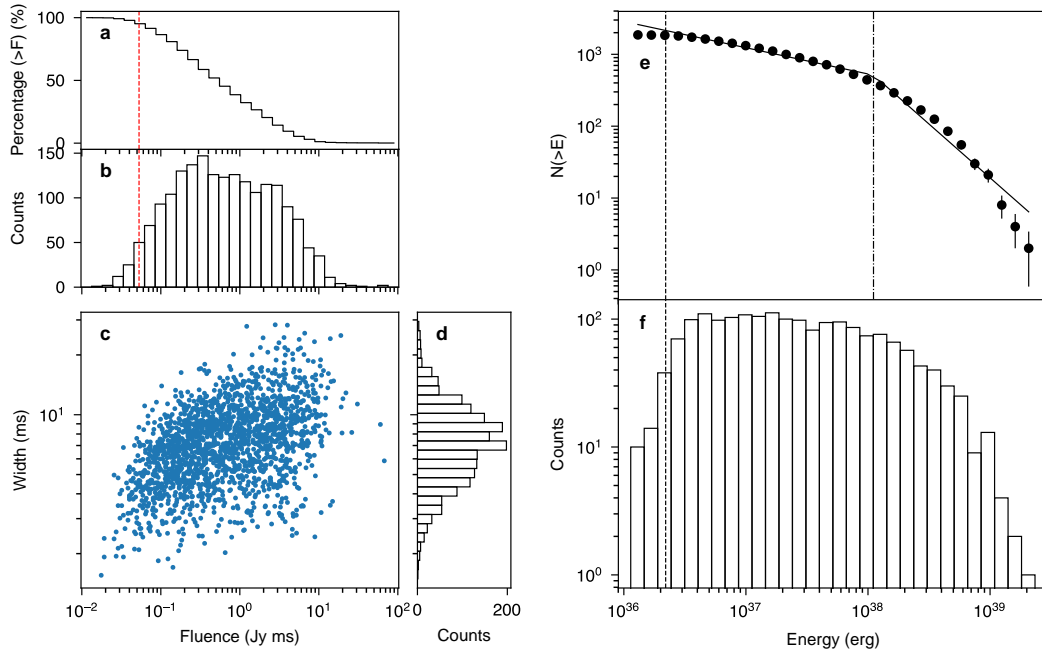
S. Dong (E-mail: dongsubo@pku.edu.cn)

W. W. Zhu (E-mail: zhuww@nao.cas.cn)

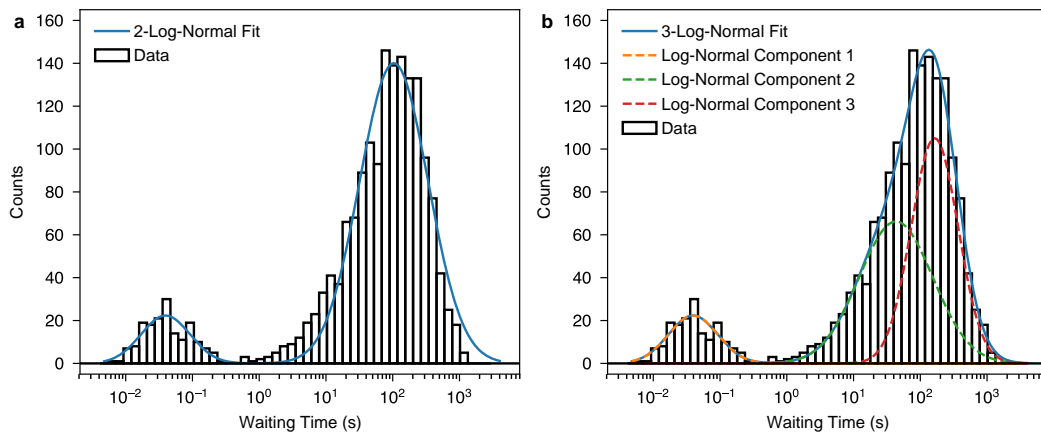
B. Zhang (Email: bing.zhang@unlv.edu)



**Extended Data Figure 1: Temporal variations of extra physical parameters.** (a) Shape parameter ( $k$ ) of Weibull distribution in event-rate inference. The error bar is at 68% confidence level. (b) and (c) Daily burst energy and DM, where the violin symbol indicates the distribution function, the green shaded strips indicate the 95% upper and lower bounds, and the solid black curve is the median.

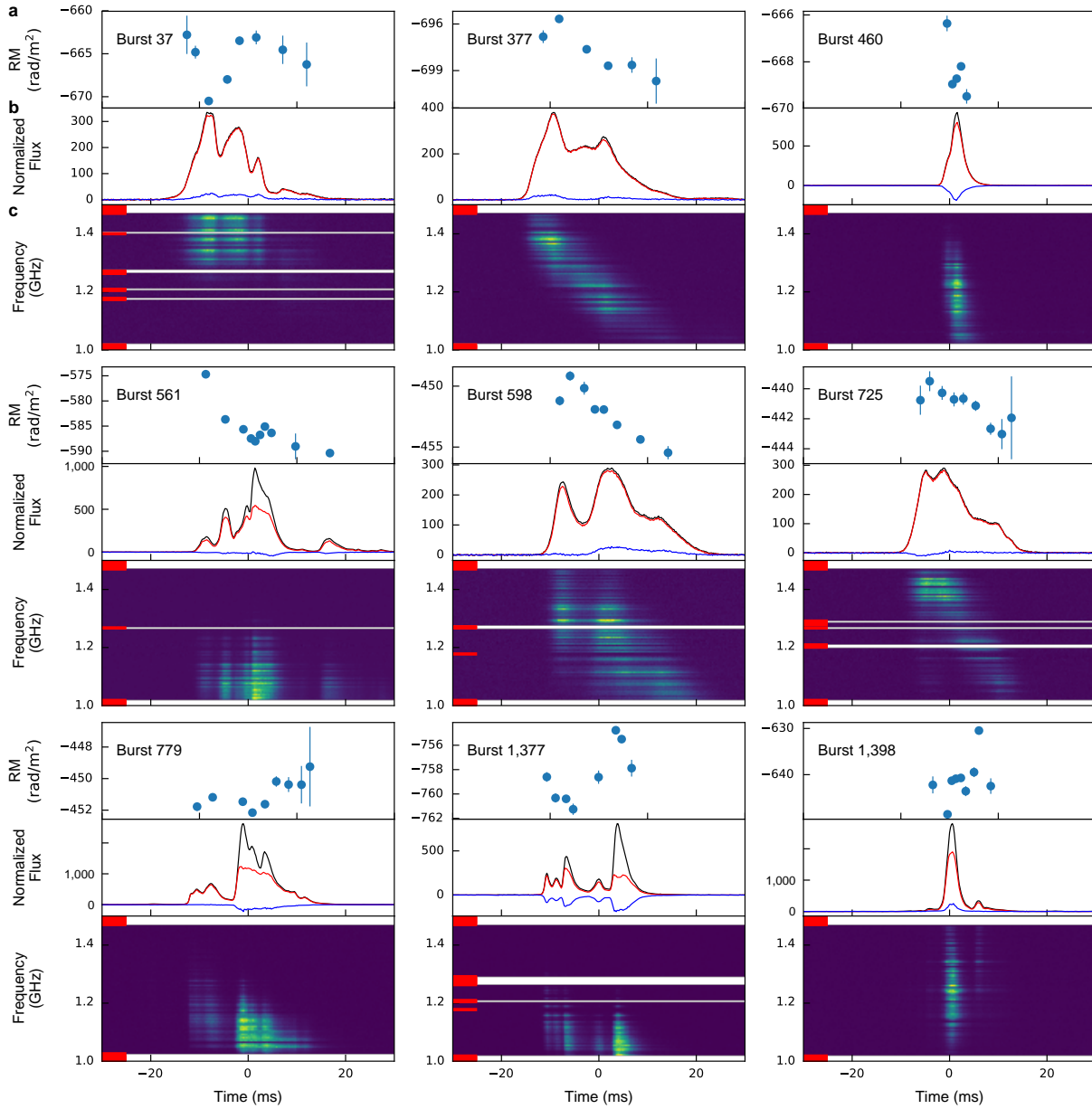


**Extended Data Figure 2: Fluence, equivalent width, and energy distribution for detected bursts.** (a) and (b) Cumulative distribution and histogram of the burst fluence; the red dashed vertical line at 53 mJy ms indicates the 95% completeness threshold. (c) The 2D distribution of fluence and burst width. (d) Histogram of burst width. (e) and (f) Cumulative distribution and histogram of FRB 20201124A burst energy; the black dashed vertical line at  $2 \times 10^{36}$  erg indicates 95% completeness assuming a burst bandwidth of 185 MHz, the median of the burst bandwidths. The broken power-law fit to the cumulative distribution of energy is the solid black curve, with the break point at  $1.1 \times 10^{38}$  erg indicated by a dot-dashed vertical line.

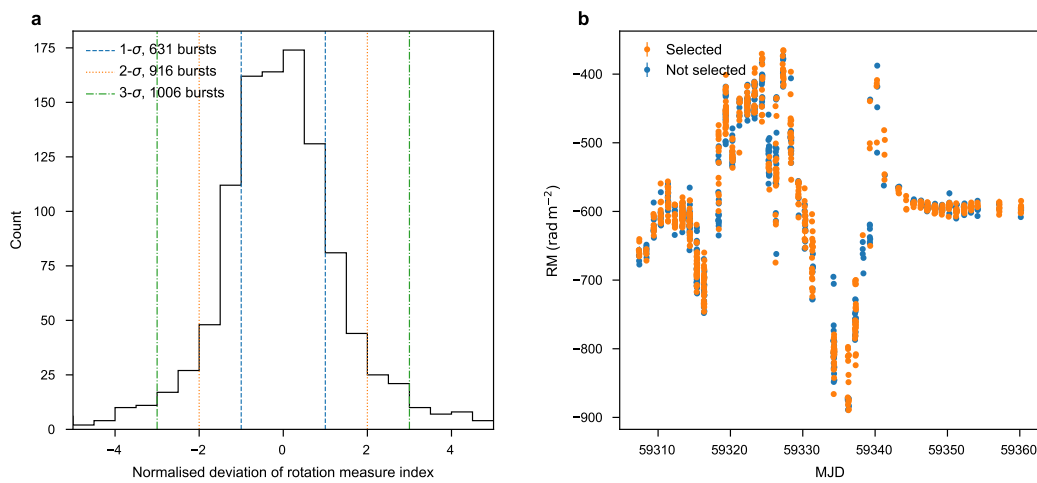


**Extended Data Figure 3: Waiting time distribution of FRB 20201124A.** (a) The best fit using two log-normal functions (the blue curve), where the two log-normal distributions peak at 39 ms and 106.7 s. (b) The best fit (blue curve) using three log-normal functions, which were indicated with the dashed-line curves, peak at 39 ms, 45.1 s, and 162.3 s.

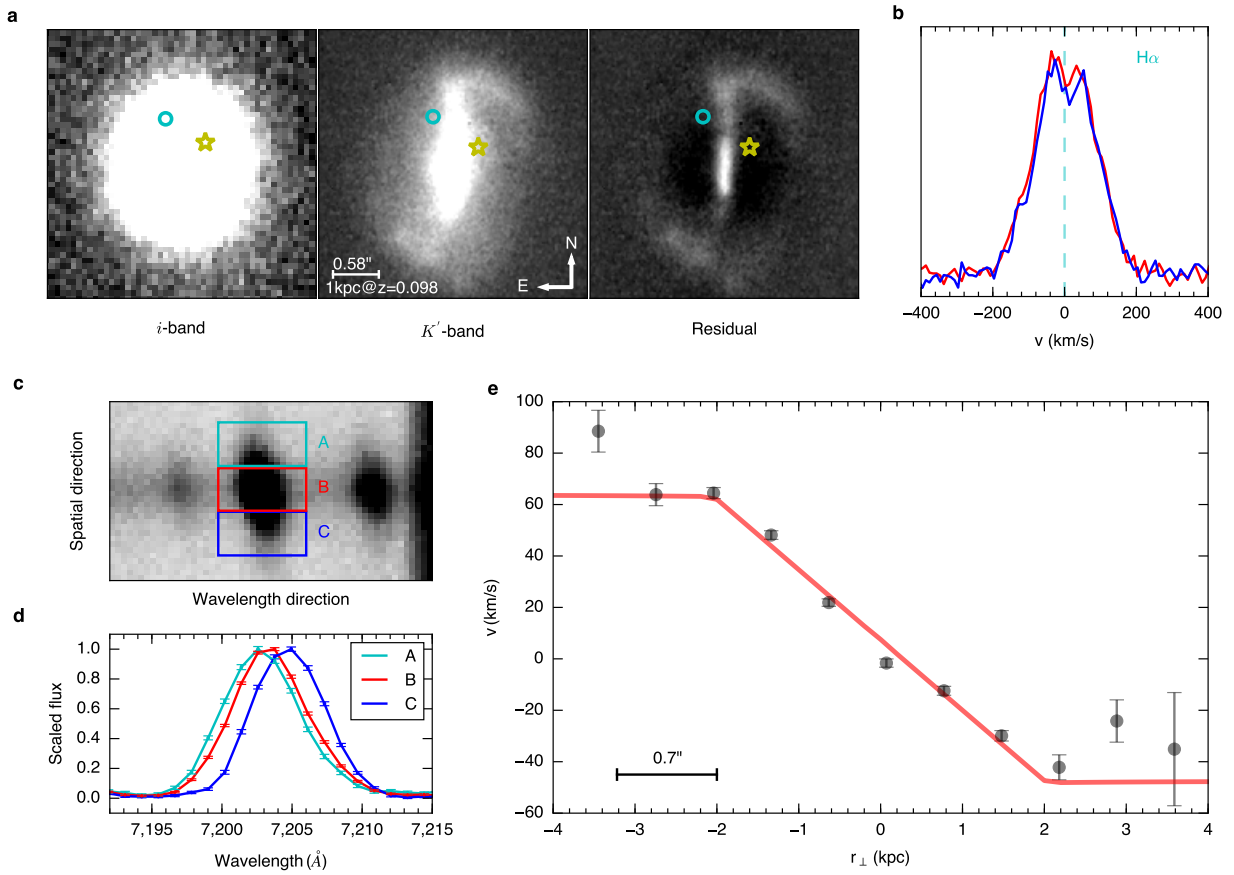




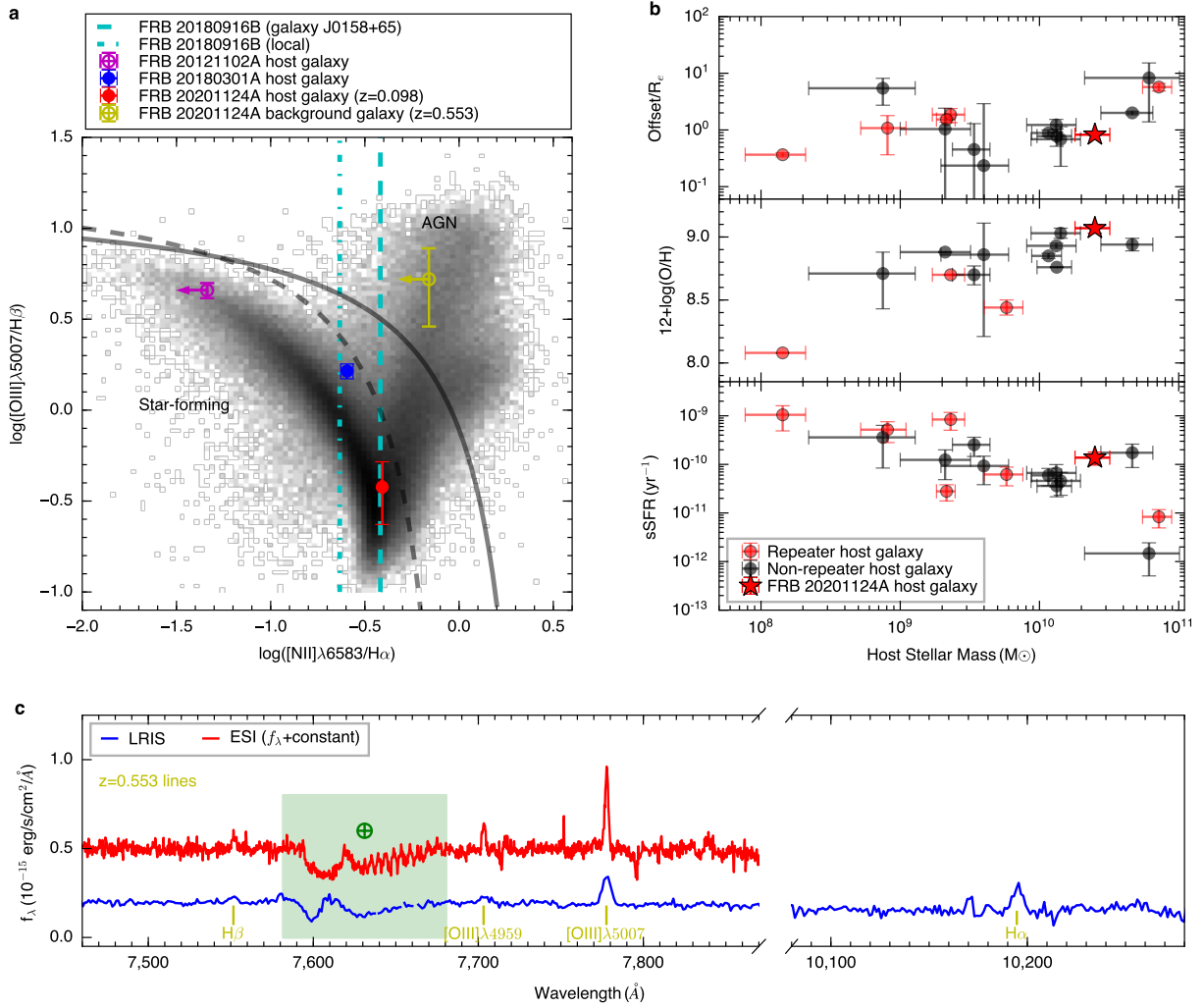
**Extended Data Figure 4: Apparent RM variation within individual bursts.** (a) RM curve with 95% confidence level error bars, (b) polarisation profiles, and (c) dynamic spectra. Bursts are dedispersed using corresponding structure-optimised DM values.



**Extended Data Figure 5: Rotation measure index.** (a) Histogram of normalised rotation measure index deviation defined as  $(\beta - 2)/\sigma_\beta$ , where  $\sigma_\beta$  is the uncertainty of  $\beta$  with 68% confidence level. (b) RM as a function of time. Orange dots are for selected bursts with  $(\beta - 2)/\sigma_\beta \leq 1$ , and the measurements not selected are in blue dots.



**Extended Data Figure 6: Properties of the host galaxy at  $z = 0.098$  in the optical and near-infrared.** (a)  $i$ -band and  $K'$ -band FRB 20201124A host-galaxy images by LRIS and NIRC2, respectively, and the residual  $K'$ -band image after subtracting the disc component. The EVN localisation of FRB 20201124A is indicated with the cyan circle, which is in 60 mas radius, i.e. 4 times the uncertainty. The centre of the background galaxy ( $z = 0.553$ ) is shown as the yellow asterisk. (b) The  $H\alpha$  double-peaked profile revealed in the medium-resolution ESI spectrum. Blue and red are for two different orders of the echelle spectrum. (c) 2D spectroscopic image by LRIS around the  $H\alpha$  emission line. A wavelength-dependent variation is clearly seen in the spatial direction. (d) The  $H\alpha$  lines extracted from three different regions, which correspond to the three rectangles in panel (c) of the galaxy along the slit. (e) The velocities at different projected distances in the slit direction relative to the continuum centre. The red line is the best-fit result of a simple rotation model. The LRIS spectroscopic observations were taken with seeing of  $0.7''$  (black bar), which sets the spatial resolution.



**Extended Data Figure 7: Properties of the galaxies and comparisons with other FRB hosts**  
**(a)** FRB repeaters’ hosts in the BPT diagram plotted with the SDSS DR8 MPA-JHU sample (black); parameter spaces of galaxies dominated by star formation and active galactic nuclei are separated by the black dashed and solid lines, respectively<sup>88,89</sup>. The host and background galaxies of FRB 2020124A are shown in red and yellow, respectively. **(b)** The properties (FRB–galaxy offset in units of galaxy effective radius  $R_e$ , gas-phase metallicity, sSFR, and stellar mass) of the FRB 20201124A host galaxy (red star) compared with a literature sample of FRB hosts (available at <https://web.archive.org/web/20211015143528/https://frbhosts.org/#explore>) shown with dots (black, non-repeaters; red, repeaters). **(c)** Emission lines from the background galaxy at  $z = 0.553$  in the LRIS (blue) and ESI (red) spectra with regions contaminated by Earth’s atmosphere marked in green.

1. Petroff, E., Hessels, J. W. T. & Lorimer, D. R. Fast radio bursts. *Astron. Astrophys. Rev.* **27**, 4 (2019).
2. Cordes, J. M. & Chatterjee, S. Fast Radio Bursts: An Extragalactic Enigma. *Ann. Rev. Astron. Astrophys.* **57**, 417–465 (2019).
3. Zhang, B. The physical mechanisms of fast radio bursts. *Nature* **587**, 45–53 (2020).
4. CHIME/FRB Collaboration et al. A bright millisecond-duration radio burst from a Galactic magnetar. *Nature* **587**, 54–58 (2020).
5. Bochenek, C. D. et al. A fast radio burst associated with a Galactic magnetar. *Nature* **587**, 59–62 (2020).
6. Li, C. K. et al. HXMT identification of a non-thermal X-ray burst from SGR J1935+2154 and with FRB 200428. *Nature Astronomy* **5**, 378 (2021).
7. Ridnaia, A. et al. A peculiar hard X-ray counterpart of a Galactic fast radio burst. *Nature Astronomy* **5**, 372–377 (2021).
8. Mereghetti, S. et al. INTEGRAL Discovery of a Burst with Associated Radio Emission from the Magnetar SGR 1935+2154. *Astrophys. J. Lett.* **898**, L29 (2020).
9. Lanman, A. E. et al. A Sudden Period of High Activity from Repeating Fast Radio Burst 20201124A. *Astrophys. J.* **927**, 59 (2022).
10. Fong, W.-f. et al. Chronicling the Host Galaxy Properties of the Remarkable Repeating FRB 20201124A. *Astrophys. J. Lett.* **919**, L23 (2021).
11. Ravi, V. et al. The host galaxy and persistent radio counterpart of FRB 20201124A. *Mon. Not. R. Astron. Soc.* **513**, 982–990 (2022).
12. Piro, L. et al. The fast radio burst FRB 20201124A in a star-forming region: Constraints to the progenitor and multiwavelength counterparts. *Astron. Astrophys.* **656**, L15 (2021).
13. Jiang, P. et al. Commissioning progress of the FAST. *Sci. China Phys. Mech. Astron.* **62**, 959502 (2019).
14. Li, D. et al. A bimodal burst energy distribution of a repeating fast radio burst source. *Nature* **598**, 267–271 (2021).
15. Hilmarsson, G. H., Spitler, L. G., Main, R. A. & Li, D. Z. Polarization properties of FRB 20201124A from detections with the Effelsberg 100-m radio telescope. *Mon. Not. R. Astron. Soc.* **508**, 5354–5361 (2021).

16. Michilli, D. *et al.* An extreme magneto-ionic environment associated with the fast radio burst source FRB 121102. *Nature* **553**, 182–185 (2018).
17. Luo, R. *et al.* Diverse polarization angle swings from a repeating fast radio burst source. *Nature* **586**, 693–696 (2020).
18. Kumar, P. *et al.* Circularly polarized radio emission from the repeating fast radio burst source FRB 20201124A. *Mon. Not. R. Astron. Soc.* **512**, 3400–3413 (2022).
19. Kramer, M., Stappers, B. W., Jessner, A., Lyne, A. G. & Jordan, C. A. Polarized radio emission from a magnetar. *Mon. Not. R. Astron. Soc.* **377**, 107–119 (2007).
20. Kumar, P., Lu, W. & Bhattacharya, M. Fast radio burst source properties and curvature radiation model. *Mon. Not. R. Astron. Soc.* **468**, 2726–2739 (2017).
21. Yang, Y.-P. & Zhang, B. Bunching Coherent Curvature Radiation in Three-dimensional Magnetic Field Geometry: Application to Pulsars and Fast Radio Bursts. *Astrophys. J.* **868**, 31 (2018).
22. Hilmarsson, G. H. *et al.* Rotation Measure Evolution of the Repeating Fast Radio Burst Source FRB 121102. *Astrophys. J. Lett.* **908**, L10 (2021).
23. Johnston, S., Ball, L., Wang, N. & Manchester, R. N. Radio observations of PSR B1259-63 through the 2004 periastron passage. *Mon. Not. R. Astron. Soc.* **358**, 1069–1075 (2005).
24. Piro, A. L. & Gaensler, B. M. The Dispersion and Rotation Measure of Supernova Remnants and Magnetized Stellar Winds: Application to Fast Radio Bursts. *Astrophys. J.* **861**, 150 (2018).
25. Metzger, B. D., Margalit, B. & Sironi, L. Fast radio bursts as synchrotron maser emission from decelerating relativistic blast waves. *Mon. Not. R. Astron. Soc.* **485**, 4091–4106 (2019).
26. Planck Collaboration *et al.* Planck 2015 results. XIII. Cosmological parameters. *Astron. Astrophys.* **594**, A13 (2016).
27. Chatterjee, S. *et al.* A direct localization of a fast radio burst and its host. *Nature* **541**, 58–61 (2017).
28. Marcote, B. *et al.* A repeating fast radio burst source localized to a nearby spiral galaxy. *Nature* **577**, 190–194 (2020).

29. Bhandari, S. *et al.* Characterizing the Fast Radio Burst Host Galaxy Population and its Connection to Transients in the Local and Extragalactic Universe. *Astron. J.* **163**, 69 (2022).
30. Baldwin, J. A., Phillips, M. M. & Terlevich, R. Classification parameters for the emission-line spectra of extragalactic objects. *Publ. Astron. Soc. Pac.* **93**, 5–19 (1981).
31. Bhandari, S. *et al.* The Host Galaxies and Progenitors of Fast Radio Bursts Localized with the Australian Square Kilometre Array Pathfinder. *Astrophys. J. Lett.* **895**, L37 (2020).
32. Li, Y. & Zhang, B. A Comparative Study of Host Galaxy Properties between Fast Radio Bursts and Stellar Transients. *Astrophys. J. Lett.* **899**, L6 (2020).
33. Tendulkar, S. P. *et al.* The Host Galaxy and Redshift of the Repeating Fast Radio Burst FRB 121102. *Astrophys. J. Lett.* **834**, L7 (2017).
34. Metzger, B. D., Berger, E. & Margalit, B. Millisecond Magnetar Birth Connects FRB 121102 to Superluminous Supernovae and Long-duration Gamma-Ray Bursts. *Astrophys. J.* **841**, 14 (2017).
35. Nimmo, K. *et al.* Milliarcsecond Localization of the Repeating FRB 20201124A. *Astrophys. J. Lett.* **927**, L3 (2022).
36. Jiang, P. *et al.* The fundamental performance of FAST with 19-beam receiver at L band. *Res. Astron. Astrophys.* **20**, 064 (2020).
37. CHIME/FRB Collaboration. Recent high activity from a repeating Fast Radio Burst discovered by CHIME/FRB. *The Astronomer's Telegram* **14497**, 1 (2021).
38. Xu, H. *et al.* FAST detection and localization of FRB20201124A. *The Astronomer's Telegram* **14518**, 1 (2021).
39. Zhang, C. F. *et al.* Fast radio burst detection in the presence of coloured noise. *Mon. Not. R. Astron. Soc.* **503**, 5223–5231 (2021).
40. Men, Y. P. *et al.* Piggyback search for fast radio bursts using Nanshan 26 m and Kunming 40 m radio telescopes - I. Observing and data analysis systems, discovery of a mysterious peryton. *Mon. Not. R. Astron. Soc.* **488**, 3957–3971 (2019).
41. Oppermann, N., Yu, H.-R. & Pen, U.-L. On the non-Poissonian repetition pattern of FRB121102. *Mon. Not. R. Astron. Soc.* **475**, 5109–5115 (2018).

42. Feroz, F., Hobson, M. P. & Bridges, M. MULTINEST: an efficient and robust Bayesian inference tool for cosmology and particle physics. Mon. Not. R. Astron. Soc. **398**, 1601–1614 (2009).
43. CHIME/FRB Collaboration et al. Periodic activity from a fast radio burst source. Nature **582**, 351–355 (2020).
44. Zou, J.-H. et al. Periodicity Search on X-Ray Bursts of SGR J1935+2154 Using 8.5 yr of Fermi/GBM Data. Astrophys. J. Lett. **923**, L30 (2021).
45. Cai, C. et al. Search for gamma-ray bursts and gravitational wave electromagnetic counterparts with High Energy X-ray Telescope of Insight-HXMT. Mon. Not. R. Astron. Soc. **508**, 3910–3920 (2021).
46. Hobbs, G. B., Edwards, R. T. & Manchester, R. N. TEMPO2, a new pulsar-timing package - I. An overview. Mon. Not. R. Astron. Soc. **369**, 655–672 (2006).
47. Cordes, J. M. & Lazio, T. J. W. NE2001.I. A New Model for the Galactic Distribution of Free Electrons and its Fluctuations. arXiv e-prints astro-ph/0207156 (2002). [astro-ph/0207156](https://arxiv.org/abs/astro-ph/0207156).
48. Yao, J. M., Manchester, R. N. & Wang, N. A New Electron-density Model for Estimation of Pulsar and FRB Distances. Astrophys. J. **835**, 29 (2017).
49. Dolag, K., Gaensler, B. M., Beck, A. M. & Beck, M. C. Constraints on the distribution and energetics of fast radio bursts using cosmological hydrodynamic simulations. Mon. Not. R. Astron. Soc. **451**, 4277–4289 (2015).
50. Deng, W. & Zhang, B. Cosmological Implications of Fast Radio Burst/Gamma-Ray Burst Associations. Astrophys. J. Lett. **783**, L35 (2014).
51. Luo, R., Lee, K., Lorimer, D. R. & Zhang, B. On the normalized FRB luminosity function. Mon. Not. R. Astron. Soc. **481**, 2320–2337 (2018).
52. Hotan, A. W., van Straten, W. & Manchester, R. N. PSRCHIVE and PSRFITS: An Open Approach to Radio Pulsar Data Storage and Analysis. Publ. Astron. Soc. Aust. **21**, 302–309 (2004).
53. Desvignes, G. et al. Radio emission from a pulsar’s magnetic pole revealed by general relativity. Science **365**, 1013–1017 (2019).



54. Sotomayor-Beltran, C. *et al.* Calibrating high-precision Faraday rotation measurements for LOFAR and the next generation of low-frequency radio telescopes. *Astron. Astrophys.* **552**, A58 (2013).
55. Welter, G. L., Perry, J. J. & Kronberg, P. P. The rotation measure distribution of QSOs and of intervening clouds :magnetic fields and column densities. *Astrophys. J.* **279**, 19–39 (1984).
56. Akahori, T., Ryu, D. & Gaensler, B. M. Fast Radio Bursts as Probes of Magnetic Fields in the Intergalactic Medium. *Astrophys. J.* **824**, 105 (2016).
57. Xu, J. & Han, J. L. Redshift evolution of extragalactic rotation measures. *Mon. Not. R. Astron. Soc.* **442**, 3329–3337 (2014).
58. Noutsos, A., Karastergiou, A., Kramer, M., Johnston, S. & Stappers, B. W. Phase-resolved Faraday rotation in pulsars. *Mon. Not. R. Astron. Soc.* **396**, 1559–1572 (2009).
59. Cho, H. *et al.* Spectropolarimetric Analysis of FRB 181112 at Microsecond Resolution: Implications for Fast Radio Burst Emission Mechanism. *Astrophys. J. Lett.* **891**, L38 (2020).
60. Mezger, P. G. & Henderson, A. P. Galactic H II Regions. I. Observations of Their Continuum Radiation at the Frequency 5 GHz. *Astrophys. J.* **147**, 471 (1967).
61. Hessels, J. W. T. *et al.* FRB 121102 Bursts Show Complex Time-Frequency Structure. *Astrophys. J. Lett.* **876**, L23 (2019).
62. Vedantham, H. K. & Ravi, V. Faraday conversion and magneto-ionic variations in fast radio bursts. *Mon. Not. R. Astron. Soc.* **485**, L78–L82 (2019).
63. Lomb, N. R. Least-Squares Frequency Analysis of Unequally Spaced Data. *Astrophys. Space Sci.* **39**, 447–462 (1976).
64. Sazonov, V. N. Generation and Transfer of Polarized Synchrotron Radiation. *Soviet astron.* **13**, 396 (1969).
65. Huang, L. & Shcherbakov, R. V. Faraday conversion and rotation in uniformly magnetized relativistic plasmas. *Mon. Not. R. Astron. Soc.* **416**, 2574–2592 (2011).
66. Beniamini, P., Kumar, P. & Narayan, R. Faraday depolarization and induced circular polarization by multipath propagation with application to FRBs. *Mon. Not. R. Astron. Soc.* **510**, 4654–4668 (2022).

67. Oke, J. B. *et al.* The Keck Low-Resolution Imaging Spectrometer. Publ. Astron. Soc. Pac. **107**, 375 (1995).
68. Rockosi, C. *et al.* The low-resolution imaging spectrograph red channel CCD upgrade: fully depleted, high-resistivity CCDs for Keck. In McLean, I. S., Ramsay, S. K. & Takami, H. (eds.) Ground-based and Airborne Instrumentation for Astronomy III, vol. 7735 of Society of Photo-Optical Instrumentation Engineers (SPIE) Conference Series, 77350R (2010).
69. Sheinis, A. I. *et al.* ESI, a New Keck Observatory Echellette Spectrograph and Imager. Publ. Astron. Soc. Pac. **114**, 851–865 (2002).
70. Perley, D. A. Fully Automated Reduction of Longslit Spectroscopy with the Low Resolution Imaging Spectrometer at the Keck Observatory. Publ. Astron. Soc. Pac. **131**, 084503 (2019).
71. Flewelling, H. A. *et al.* The Pan-STARRS1 Database and Data Products. Astrophys. J., Suppl. Ser. **251**, 7 (2020).
72. Cardelli, J. A., Clayton, G. C. & Mathis, J. S. The Relationship between Infrared, Optical, and Ultraviolet Extinction. Astrophys. J. **345**, 245 (1989).
73. Schlafly, E. F. & Finkbeiner, D. P. Measuring Reddening with Sloan Digital Sky Survey Stellar Spectra and Recalibrating SFD. Astrophys. J. **737**, 103 (2011).
74. Filippenko, A. V. The importance of atmospheric differential refraction in spectrophotometry. Publ. Astron. Soc. Pac. **94**, 715–721 (1982).
75. Wizinowich, P. L. *et al.* The W. M. Keck Observatory Laser Guide Star Adaptive Optics System: Overview. Publ. Astron. Soc. Pac. **118**, 297–309 (2006).
76. Gaia Collaboration *et al.* Gaia Data Release 2. The celestial reference frame (Gaia-CRF2). Astron. Astrophys. **616**, A14 (2018).
77. Calzetti, D. *et al.* The Dust Content and Opacity of Actively Star-forming Galaxies. Astrophys. J. **533**, 682–695 (2000).
78. Heintz, K. E. *et al.* Host Galaxy Properties and Offset Distributions of Fast Radio Bursts: Implications for Their Progenitors. Astrophys. J. **903**, 152 (2020).
79. Belfiore, F. *et al.* SDSS IV MaNGA - sSFR profiles and the slow quenching of discs in green valley galaxies. Mon. Not. R. Astron. Soc. **477**, 3014–3029 (2018).

80. Blanc, G. A., Kewley, L., Vogt, F. P. A. & Dopita, M. A. IZI: Inferring the Gas Phase Metallicity ( $Z$ ) and Ionization Parameter ( $q$ ) of Ionized Nebulae Using Bayesian Statistics. *Astrophys. J.* **798**, 99 (2015).
81. Mingozi, M. et al. SDSS IV MaNGA: Metallicity and ionisation parameter in local star-forming galaxies from Bayesian fitting to photoionisation models. *Astron. Astrophys.* **636**, A42 (2020).
82. Peng, C. Y., Ho, L. C., Impey, C. D. & Rix, H.-W. Detailed Decomposition of Galaxy Images. II. Beyond Axisymmetric Models. *Astron. J.* **139**, 2097–2129 (2010).
83. Holmberg, E. A photographic photometry of extragalactic nebulae. *Meddelanden fran Lunds Astronomiska Observatorium Serie II* **136**, 1 (1958).
84. Tully, R. B. & Fisher, J. R. A new method of determining distances to galaxies. *Astron. Astrophys.* **500**, 105–117 (1977).
85. Ouellette, N. N. Q. et al. The Spectroscopy and H-band Imaging of Virgo Cluster Galaxies (SHIVir) Survey: Scaling Relations and the Stellar-to-total Mass Relation. *Astrophys. J.* **843**, 74 (2017).
86. Law, D. R. et al. SDSS-IV MaNGA: Refining Strong Line Diagnostic Classifications Using Spatially Resolved Gas Dynamics. *Astrophys. J.* **915**, 35 (2021).
87. Main, R. A. et al. Scintillation time-scale measurement of the highly active FRB20201124A. *Mon. Not. R. Astron. Soc.* **509**, 3172–3180 (2022).
88. Kewley, L. J., Dopita, M. A., Sutherland, R. S., Heisler, C. A. & Trevena, J. Theoretical Modeling of Starburst Galaxies. *Astrophys. J.* **556**, 121–140 (2001).
89. Kauffmann, G. et al. The host galaxies of active galactic nuclei. *Mon. Not. R. Astron. Soc.* **346**, 1055–1077 (2003).